Title: Global Biosphere Productivity Response to Atlantic Meridional Overturning Circulation Collapse During Heinrich Stadial 4

Authors

Ji-Woong Yang[1,2*], Jean-Baptiste Ladant[1], Thomas Blunier[2], Amaëlle Landais[1], Masa Kageyama[1], Didier Paillard[1], Nicolas Viovy[1], Pascale Braconnot[1], María Fernanda Sánchez Goñi[3], Frédéric Prié[1], Sébastien Nguyen[1], Louise Crinella-Morici[1]†

Affiliations

[1]Université Paris-Saclay, CNRS, CEA, UVSQ, Laboratoire des Sciences du Climat et de l'Environnement, 91191 Gif-sur-Yvette, France.

[2]Physics of Ice, Climate, and Earth, Niels Bohr Institute, University of Copenhagen, 2200 Copenhagen, Denmark

[3]Environnements et Paléoenvironnements Océaniques et Continentaux, Université de Bordeaux, EPHE, Université PSL, CNRS, 33614 Pessac, France

†present address : Centre de Recherches Pétrographiques et Géochimiques, Université de Lorraine, CNRS, 54000 Nancy, France

Correspondence: Ji-Woong Yang (ji-woong.yang@lsce.ipsl.fr)

This is a non-peer-reviewed preprint submitted to Science Advances.

FRONT MATTER

Title

- Global Biosphere Productivity Response to Atlantic Meridional Overturning Circulation Collapse During Heinrich Stadial 4
- Global Biosphere Productivity during Heinrich Stadial 4

Authors

Ji-Woong Yang[1,2*], Jean-Baptiste Ladant[1], Thomas Blunier[2], Amaëlle Landais[1], Masa Kageyama[1], Didier Paillard[1], Nicolas Viovy[1], Pascale Braconnot[1], María Fernanda Sánchez Goñi[3], Frédéric Prié[1], Sébastien Nguyen[1], Louise Crinella-Morici[1]†

Affiliations

[1]Université Paris-Saclay, CNRS, CEA, UVSQ, Laboratoire des Sciences du Climat et de l'Environnement, 91191 Gif-sur-Yvette, France.

[2]Physics of Ice, Climate, and Earth, Niels Bohr Institute, University of Copenhagen, 2200 Copenhagen, Denmark

[3]Environnements et Paléoenvironnements Océaniques et Continentaux, Université de Bordeaux, EPHE, Université PSL, CNRS, 33614 Pessac, France

†present address : Centre de Recherches Pétrographiques et Géochimiques, Université de Lorraine, CNRS, 54000 Nancy, France

Abstract

The slowdown of the Atlantic Meridional Overturning Circulation (AMOC) due to ongoing climate change raises concerns about its impact on the global carbon cycle. Understanding how global biosphere productivity may respond to such changes is essential for predicting the future carbon cycle, yet quantifying past global biosphere productivity remains challenging. We use triple isotope composition of air oxygen ($^{17}\Delta$) trapped in polar ice cores to reconstruct the global biosphere productivity over the period 40.5 to 38.6 thousand years ago (ka BP), covering Heinrich Stadial 4 (HS4), a period of weakened AMOC. Our data reveal a slight increase in productivity following a CO_2 rise around 39.5 ka BP. Freshwater hosing experiments using a global climate model indicate that the CO_2 fertilization effect on the terrestrial biosphere offsets productivity declines caused by consequences of AMOC slowdown. Collectively, our results suggest that global biosphere productivity is slightly increases in response to AMOC slowdown.

Teaser

Global biosphere productivity likely increases in response to abrupt climate change caused by slowdown of ocean circulation.

MAIN TEXT

Introduction

Oxygenic photosynthesis in both terrestrial and oceanic biospheres is fundamental to life on Earth, as it converts light energy and inorganic carbon into organic matter essential for sustaining ecosystems (*e.g., 1*). As the largest flux of carbon between the atmosphere and the biosphere (*e.g., 2*), photosynthesis has played a pivotal role in shaping Earth's atmosphere and climate by fixing atmospheric carbon dioxide (CO_2) and releasing molecular oxygen (O_2) to the atmosphere (*e.g., 3*, *4*). However, global photosynthesis is itself affected by Earth's climate. Field measurements and satellite observation over recent decades have shown that the global (land and ocean) rate of photosynthesis has varied along with global climate change, being constrained by various climatic- and environmental factors (*e.g., 2*, *5*, *6*, *7*). Understanding mechanisms by which global photosynthesis responds to climate change will provide invaluable insight into the future dynamics of the global O_2 and carbon cycles.

A major threat of ongoing climate change is a slowdown or eventual shut down of the Atlantic Meridional Overturning Circulation (AMOC) (*e.g., 8, 9*). Weakened AMOC will result in major climatic and hydrological changes at global scale (*e.g., 10-12*), likely affecting the biological O_2 cycle through changes in both photosynthesis and respiration in global biosphere. Projections for a collapse of the AMOC are ranging from not before 2100 (*13*) to as early as the mid-XXIst century (*9*). Numerous studies – using global climate models (GCMs) – have been dedicated to projecting the response of the terrestrial- and marine biosphere to the anticipated slowdown of AMOC (*e.g.,14*). Nevertheless, the ability of most GCMs to simulate the photosynthesis in global biosphere have not yet been validated under climate boundary conditions different from those of the pre-industrial period.

Slowdowns of the AMOC have occurred on several occasions in the past, providing an opportunity to investigate the potential impacts of such changes in the future. Water stable isotope ratios measured from Greenland ice cores reveal multiple shifts between cold and warm intervals during the last glacial period, namely Dansgaard-Oeschger (DO) events (*e.g., 15*), while Antarctic ice core records show gradual warming and cooling, respectively (*e.g., 16, 17*). The asynchronous coupling between temperature evolutions at both poles has been explained by the bipolar-seesaw mechanism, invoking redistribution of heat between Northern and Southern Hemisphere due to changes in AMOC (*18*, *19*). According to this mechanism, during Greenland cold phases (stadials), reduced heat transport from the Southern Hemisphere (SH) to the Northern Hemisphere (NH) due to weakened AMOC leads to cooling around the North Atlantic Ocean and warming in the SH. In response to the NH high latitude cooling the Intertropical Convergence Zone (ITCZ) migrates south modifying precipitation patterns in the tropics. Among the stadials, those associated with massive iceberg discharges into North Atlantic Ocean (i.e., Heinrich Event) are classified as Heinrich stadials (*20*) and characterized by more pronounced climate changes than other stadials. For example, geochemical tracers for past ocean circulation such as ratio of protactinium to thorium isotopes ($^{231}Pa/^{230}Th$) indicate a systematic reduction of deep-water formation in North Atlantic during stadials, of which most pronounced changes are observed during Henrich stadials (*e.g., 21*).

The reorganization of the AMOC is also thought to drive substantial changes in the global carbon cycle. Antarctic ice-core measurements show that atmospheric CO_2 concentrations increase during Heinrich stadials (HSs) but do not do so during short, non-Heinrich

stadials (*22*, *23*). Although debated, the prevailing interpretation of these millennial-scale CO_2 rises attributes them to enhanced ventilation of deep waters in the Southern Ocean, likely driven by intensified westerly winds (*e.g., 23*). More recently, ice-core measurements of methane (CH_4) isotopic composition suggest widespread biomass burning as an additional source of carbon explaining the abrupt CO_2 rise (*24*). With a CO_2 increase of ~14 ppm, which is greater than those observed during the other HSs (*25*), the Heinrich Stadial 4 (HS4) thus provides an ideal case for examining the response of global biosphere to eventual AMOC weakening coupled with rising atmospheric CO_2.

Scientists have made a huge effort to understand the terrestrial- and ocean biosphere productivity during HS, relying either on fossil pollen assemblages or on geochemical tracers of export production measured from lacustrine- or marine sediment cores. Nonetheless, estimating the global biosphere productivity remains challenging because most of previous records are based on indirect and qualitative proxies, but also because they record local changes in biological productivity and hence demonstrate a large spatial heterogeneity. For example, a compilation of marine sediment records covering the last glacial period demonstrates a reduction of export productivity in the North Atlantic and North Pacific Oceans and an increase in the Southern Ocean and the Eastern Equatorial Pacific Ocean in response to Heinrich Events (*e.g., 26*). Modeling studies suggest that the weakening (or shutdown) of the AMOC – generally obtained by adding freshwater to the North Atlantic Ocean – leads to a reduced global terrestrial and marine primary productivity (*26-28*). However, those studies solely investigate the effect of freshwater hosing and neglect other drivers of biosphere productivity changes, specifically atmospheric CO_2 and dust deposition, which have varied across HS4.

Triple isotopic composition ($\delta^{17}O$ and $\delta^{18}O$) of air O_2 offer the possibility to directly access the global biosphere productivity (*29*, *30*). This tracer approach is based on the deviation of ^{17}O isotope from the mass-dependent fractionation and hence the triple isotopic composition of air O_2 and is reported as $^{17}\Delta \equiv \ln(\delta^{17}O+1) - \lambda_{ref} \cdot \ln(\delta^{18}O+1)$ (*31*, *32*). λ_{ref} is the slope of $\ln(\delta^{17}O+1)$ vs. $\ln(\delta^{18}O+1)$ by mass-dependent fractionation of O_2 in the biosphere under steady state, and equals to 0.516 (*32*). The O_2 produced in the biosphere (by photosynthesis) exhibits a positive $^{17}\Delta$ value relative to modern air standard in essence originating from the source water and is not much modified by other fractionation processes occurring in the biosphere (*e.g., 29*). On the other hand, the O_2 circulating through the stratosphere becomes depleted in ^{17}O by photochemical reactions that depletes ^{17}O and ^{18}O isotopes of residual O_2 in a so-called mass-independent way. The relative contribution of O_2 fluxes with distinct $^{17}\Delta$ signatures determines the $^{17}\Delta$ of tropospheric O_2, which is enclosed in bubbles in polar ice cores. Therefore, the global biosphere O_2 flux can be estimated by constraining the fractionations in the biosphere and the stratosphere as well as the stratospheric flux. Note that the global biosphere flux obtained from $^{17}\Delta$ approach represents the gross photosynthetic O_2 productivity, that is, the production rate of O_2 via splitting water molecules in Photosystem II. For simplicity, we refer to gross O_2 productivity (GOP) hereafter.

The ice-core measurements of $^{17}\Delta$ have so far been applied to reconstruct the GOP variability over glacial-interglacial cycles (*29*, *30*, *33*, *34-36*). However, the temporal resolution of previous data does not allow to estimate GOP changes at sub-millennial time scale. In this study, we attempt for the first time to reconstruct the GOP evolution during HS4 from new high-resolution measurements of $^{17}\Delta$ from the NEEM ice cores. In the following, we first describe the calculation of GOP from ice-core $^{17}\Delta$ records, and then

explore potential mechanisms of GOP change during HS4 using specifically designed coupled climate-vegetation-biogeochemistry simulations (see Materials and Methods) performed with the IPSL-CM5A2-VLR GCM (*37*).

Results

New ice-core measurements of $^{17}\Delta$ from the NEEM ice core and reconstruction of GOP

The new $^{17}\Delta$ data measured from the NEEM ice core are plotted in Figure 1. The $^{17}\Delta$ data have been corrected for isotopic fractionation due to gravitational settling in the firn column, preferential gas loss during ice-core storage, and bubble close off (see Materials and Methods). Error bars on individual data points represent the standard error of the mean from replicate measurements. We smooth the $^{17}\Delta$ records by a 1000-year moving average given the turnover time of atmospheric O_2 being ~1000 years (*38*). The 95% confidence intervals of the smoothed $^{17}\Delta$ curve are estimated from 1000 Monte-Carlo simulations using randomly perturbed $^{17}\Delta$ data. We transferred the gas chronology of the NEEM ice core (*39*) to that of WAIS Divide (WD2014) by matching CH_4 concentration records from both drilling sites (*40*, *41*).

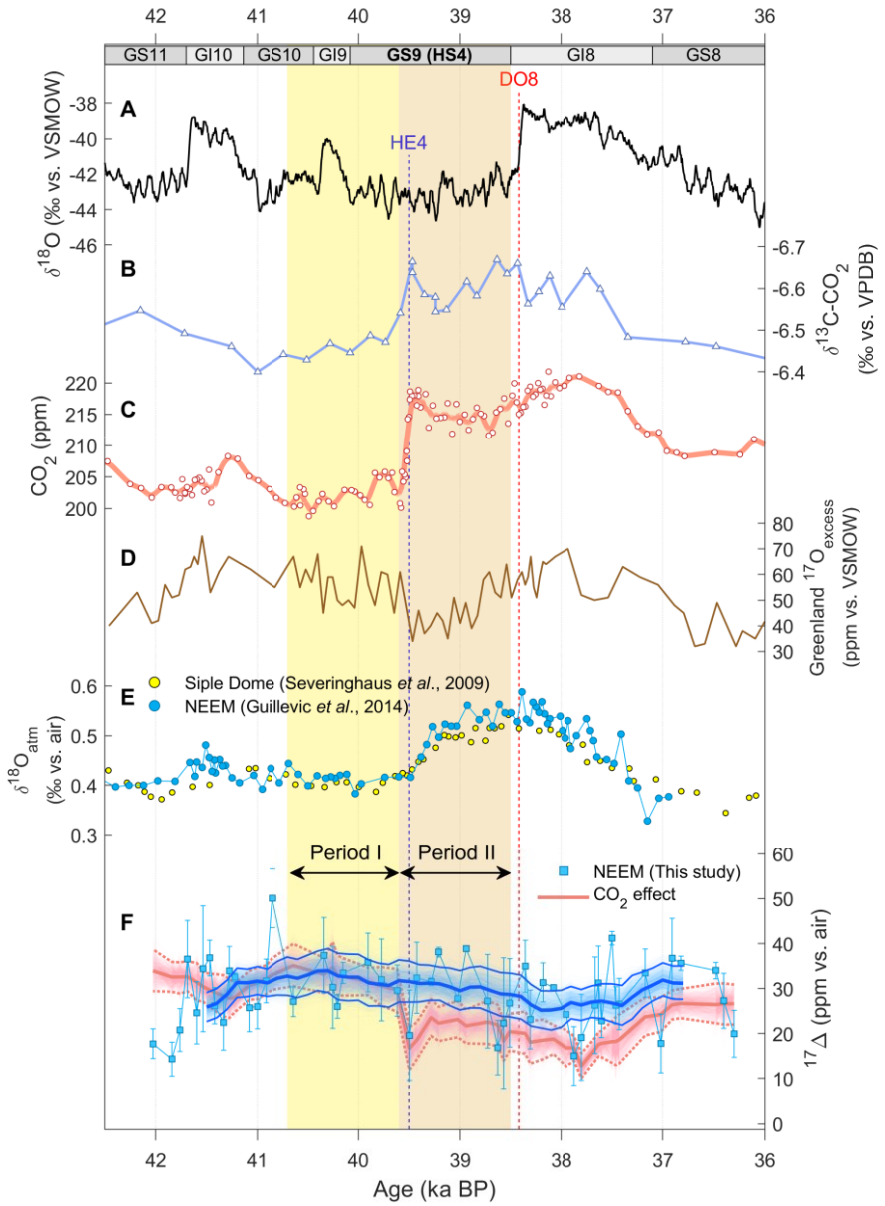

175

176 **Figure 1. Triple isotope measurements of O_2 from the NEEM ice core over HS4.** (**A**) Water stable isotope
177 records from the North Greenland Ice Core Project (NGRIP) ice core (*42*), smoothed by 50-year moving average. (**B**)
178 Stable carbon isotope ratio of CO_2 measured from Taylor Glacier (*43*). Following Wendt *et al*. (*25*), the δ^{13}C-CO_2
179 records are shifted by 160 years from its original chronology. (**C**) Atmospheric CO_2 concentration measured from the
180 WAIS-Divide ice core, Antarctica (in circles; *25*) and smoothed curve with 50-year moving average (solid line). (**D**)
181 ^{17}O-anomaly in water ($^{17}O_{excess}$) measured in NEEM ice core (*44*). (**E**) δ^{18}O of atmospheric O_2 ($\delta^{18}O_{atm}$) measured in
182 NEEM (blue; *44*) and Siple Dome (yellow; *45*) ice cores. (**F**) NEEM $^{17}\Delta$ records from NEEM ice core (blue). Error
183 bars indicate 1 standard error of the mean estimated from duplicate measurements. Also shown in pink are modelled
184 $^{17}\Delta$ curve resulting from CO_2 effect alone (see text). All data is presented on the WD2014 time scale (see Materials
185 and Methods). Yellow and orange shades indicate the 1000-year intervals before- and after the abrupt CO_2 jump,
186 corresponding to Period I and II, respectively (see text).

187

The smoothed NEEM $^{17}\Delta$ record shows no significant millennial-scale variability from the onset of GS-10 (~41 ka BP) to throughout DO-8 (~38.5 ka BP). In contrast, atmospheric CO_2 concentration exhibits an abrupt rise of ~14 ppm at 39.5 ka BP remaining elevated through DO-8 (*25*) (Figure 1). This CO_2 increase is accompanied by a sharp depletion in the carbon isotopic composition of CO_2 (δ^{13}C-CO_2), indicating a rapid injection of ^{13}C-depleted carbon into the atmosphere (*43*). Additionally, the $\delta^{18}O$ of atmospheric O_2 ($\delta^{18}O_{atm}$) becomes progressively enriched following the CO_2 rise, continuing until DO-8, likely reflecting low-latitude hydrological changes (*28*, *44-46*). To interpret our $^{17}\Delta$ data under distinct circumstances, we compare two intervals – Period I (40.6 to 39.6 ka BP; before CO_2 jump) and Period II (39.5 to 38.5 ka BP; after CO_2 jump).

The cumulative stratospheric isotope exchange reaction between O_2 and CO_2 depends on the abundance of CO_2 (*47*, *48*). Scaling the reaction accordingly (see Blunier *et al*. (*30*)), the ~14 ppm increase in CO_2 at 39.5 ka BP (between Period I and Period II in Fig. 1) depletes tropospheric $^{17}\Delta$ by 11 ± 5 ppm (1σ). For this calculation (red line in Fig. 1), all other potential influences – biological and hydrological processes – were held constant. This effect (hereafter referred to as the "CO_2-effect") must be compensated for, and in the following section, we discuss potential changes that could offset the CO_2-effect. To assess the influence of each processes, we employ a box model that captures the major fluxes and associated fractionation processes (*33*; see Materials and Methods).

In addition to the CO_2-effect, variability in the stratospheric effect (α_{str}) and influx of stratospheric O_2 into the troposphere (F_{str}) influence the tropospheric $^{17}\Delta$ signal. Balancing the tropospheric $^{17}\Delta$ signal by either a weaker α_{str} or a decrease in F_{str} is easily achievable (Fig. 2). However, the effect on $\delta^{18}O_{atm}$ of this exercise balancing $^{17}\Delta$ is neglectable, as the $^{18}\varepsilon_{str} = {}^{18}\alpha_{str}$ -1 is expected to be in the order of ~10^{-3}‰ (*49*), and thus conflicting with the observed progressive enrichment of $\delta^{18}O_{atm}$ following the CO_2 rise, continuing until DO-8. Moreover, a decrease in α_{str} with rising CO_2 appears unlikely, as the rate of oxygen isotope transfer from O_3 to CO_2 via $O(^1D)$ quenching depends on the variability of CO_2 (*48*). Also, a reduction of F_{str} seems improbable. Independent constraints derived from triple oxygen isotope measurement in ice-core nitrate (NO_3) suggest that the Brewer-Dobson circulation (BDC), the global overturning circulation responsible for the mass transport between the troposphere and the stratosphere (e.g., *50*), likely accelerated in response to enhanced latitudinal sea surface temperature (SST) gradients (*51*). Freshwater input during HS4 (Period II) likely induced significant North Atlantic cooling and thus steepened the SST gradient as also indicated by a freshwater hosing experiments using the IPSL-CM5A2-VLR model (Figure S6). Furthermore, 2-D chemistry-climate model experiments show that rising CO_2 concentrations accelerate BDC (*52*).

We conclude that stratospheric processes are insufficient to explain the observed $^{17}\Delta$ and $\delta^{18}O_{atm}$ records which leaves us with processes related to biological productivity. The biogenic $^{17}\Delta$ signature is sensitive to hydrological processes affecting the isotopic composition of leaf water, ultimately transferred to that of photosynthetic O_2. The aforementioned change in $\delta^{18}O_{atm}$ has been interpreted as a signal of low-latitude hydrological changes linked to a southward shift of the ITCZ (*28*, *44-46*) which also affects the $^{17}\Delta$ signal in precipitation water (*44*).

Increase in the $\delta^{18}O$ of precipitation water to match the observed $\delta^{18}O_{atm}$ has a limited impact on $^{17}\Delta$ (Fig. 2). Further, the results from Guillevic *et al*. (*44*) based on the Greenland NEEM ice-core measurements suggest a ~15 ppm depletion of $^{17}\Delta$ in

precipitation ($^{17}O_{excess}$) on Greenland during a southward shift of the ITCZ. Applying the 15-ppm depletion of $^{17}O_{excess}$ further depletes $^{17}\Delta$ by ~20 ppm and therefore does not counterbalance the CO_2-effect. We note however, that the Greenland $^{17}\Delta$ in precipitation water may not reflect a global trend.

Taken together, we deem it likely that an increase in GOP counterbalances the CO_2-effect, increasing the release of enriched $^{17}\Delta$ to the atmosphere. Indeed, a scenario with enhanced GOP effectively counterbalances the CO_2-effect but cannot fully account for the enrichment of $\delta^{18}O_{atm}$ (Fig. 2). The slight enrichment in $\delta^{18}O_{atm}$ under the enhanced GOP scenario results from changes in global respiration under steady-state conditions (see Materials and Methods). These results suggest that the $^{17}\Delta$ variations across HS4 can be mostly explained by increase in GOP, while the $\delta^{18}O_{atm}$ variations are primarily driven by changes in the hydrological cycle. We therefore consider a combined scenario involving changes in GOP and the hydrological cycle to be the most plausible explanation.

Based on above principle, we estimate the GOP variations from ice-core $^{17}\Delta$ and $\delta^{18}O_{atm}$ records by solving inversely our box model (see Materials and Methods). The reconstructed GOP from our 'best-guess' scenario is plotted in Figure 2. Monte-Carlo simulations (n = 3000) incorporating random perturbations with analytical uncertainty of ice-core $^{17}\Delta$ show that the mean GOP during Period II is about 2% higher than Period I (Fig. 2K). Less than 9% out of 3000 solutions indicate a decrease in GOP in Period II.

Our finding contrasts with previous modelling-based studies that suggest a decline in terrestrial biosphere GOP (*28*) and marine primary productivity (*26*) in response to AMOC slowdown. We attribute this discrepancy to the fact that those studies primarily focused on the impacts of freshwater hosing into the North Atlantic Ocean and did not account for additional factors, such as rising atmospheric CO_2 concentrations and changes in dust deposition, that may modulate or counterbalance the effects of AMOC weakening.

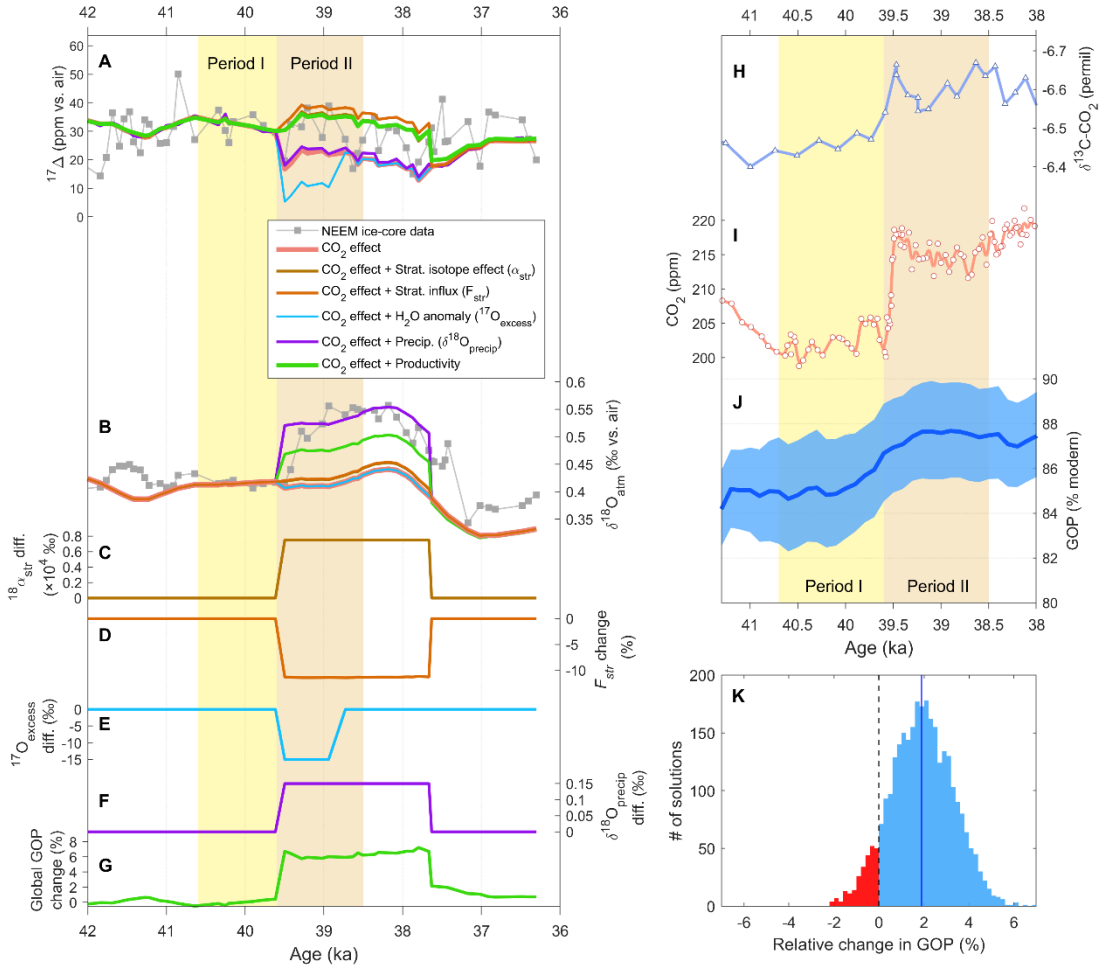

Figure 2. Modeled isotopic composition of O_2 and global biosphere productivity reconstruction. (**A** and **B**) Modelled $^{17}\Delta$ and $\delta^{18}O_{atm}$ for different scenarios compared with NEEM $^{17}\Delta$ and $\delta^{18}O_{atm}$ records (in grey). (**C** to **G**) Hypothetic time series of forcing factors used to create the modelled $^{17}\Delta$ and $\delta^{18}O_{atm}$: (**C**) change in the stratospheric isotope effect ($^{18}\alpha_{str}$), (**D**) relative change in the influx of stratospheric O_2, (**E**) change in the ^{17}O-anomaly of precipitation water consumed by terrestrial plants, (**F**) change in the $\delta^{18}O$ of precipitation water ($\delta^{18}O_{precip}$) consumed by terrestrial plants, and (**G**) relative change in global biosphere O_2 productivity. (**H**) $\delta^{13}C$-CO_2 and (**I**) CO_2 concentrations between 41 and 38 ka BP intervals. (**J**) Reconstructed GOP from NEEM $^{17}\Delta$ records, smoothed by 1000-year moving average. Blue envelops indicate 2.5 and 97.5 percentiles of 3000 Monte-Carlo simulations. Yellow and orange shades indicate Period I and II, respectively. (**K**) Histogram of relative change of GOP between Period II and Period I from 3000 Monte-Carlo simulations.

Global climate model experiments

To gain insight on the mechanisms that could drive GOP changes across HS4, we carried out five experiments using IPSL-CM5A2-VLR GCM with different set of forcing factors (see Materials and Methods for additional details). On a control experiment with boundary conditions of 40 ka BP (Ctrl_40ka), we introduce perturbations that are added incrementally on the preceding simulations (Table 1): freshwater hosing in the North Atlantic (Exp_FWF), dust forcing characteristic of an HS (Exp_DUST), CO_2 change associated with HS4 (Exp_CO2). The final simulation (Exp_VFIX) is the identical to Exp_CO2 but the vegetation cover is fixed to that obtained at the end of Ctrl_40ka. All but Exp_VFIX IPSL-CM5A2-VLR coupled model simulations are run in dynamic vegetation mode, thereby allowing plant functional types (PFTs) to evolve interactively in response to the simulated climate. We prescribe the simulated LGM (21 ka BP) dust deposition field (*56*) for Ctrl_40ka and Exp_FWF experiments and H1 (16 ka BP) dust deposition field (*57*) for Exp_DUST, Exp_CO2, and Exp_VFIX because our GCM simulation does not include an interactive aerosol module.

Table 1. List and description of the experiments conducted in this study.

Experiment	Hosing	Dust deposition	CO_2	Vegetation
Ctrl_40ka	No	LGM (21 ka BP)	200 ppm	Dynamic
Exp_FWF	Yes	LGM (21 ka BP)	200 ppm	Dynamic
Exp_DUST	Yes	H1 (16 ka BP)	200 ppm	Dynamic
Exp_CO2	Yes	H1 (16 ka BP)	210 ppm	Dynamic
Exp_VFIX	Yes	H1 (16 ka BP)	210 ppm	Fixed to Ctrl_40ka

The Ctrl_40ka experiment results in a global terrestrial- and marine GOP of 20.8 and 8.8 Pmol O_2 $year^{-1}$, respectively, yielding a global GOP of 29.6 Pmol O_2 $year^{-1}$ (Fig. 3). The 40-ka GOP obtained in our control experiment is ~84.5% of the value from the pre-industrial experiment performed with identical version of GCM (IPSL-CM5A2-VLR) (*37*). This result is in good agreement with the value obtained from ice-core $^{17}\Delta$ records.

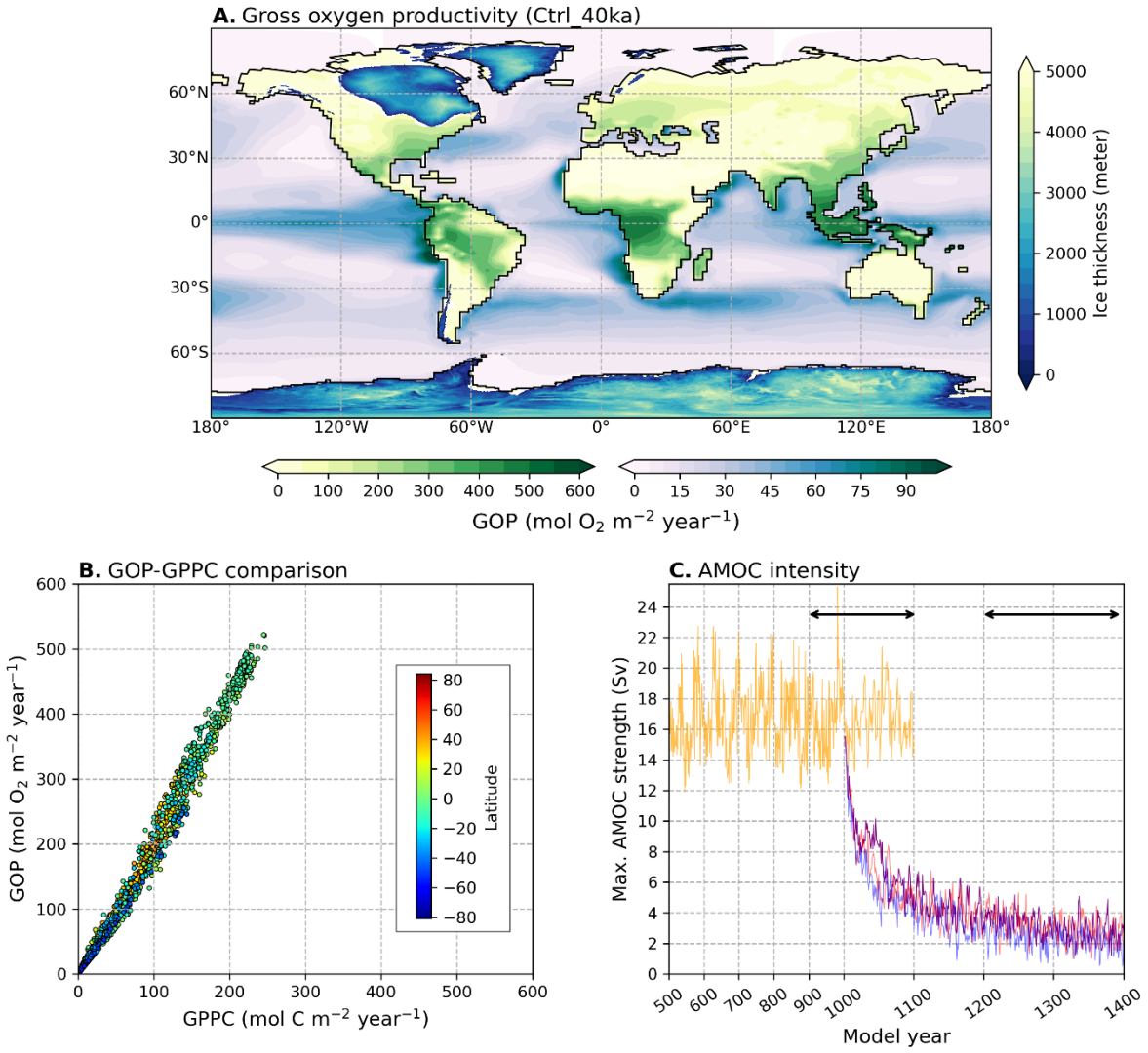

Figure 3. Gross oxygen productivity (GOP) and Atlantic meridional overturning circulation (AMOC) for 40 ka control simulation. (**A**) Global distribution of terrestrial- and marine GOP obtained in the Ctrl_40ka experiment. (**B**) Scatter plot for GOP versus gross primary productivity (GPP; mol C m^{-2} $year^{-1}$) obtained in ORCHIDEE land surface model. (**C**) Time-series of annual maximum strength of AMOC (in Sverdrup) for Ctrl_40ka experiment (yellow) and perturbation experiments (purple: Exp_CO2, red: Exp_DUST, blue: Exp_VFIX). The black arrows indicate the period of averaging for comparisons.

Effect of freshwater hosing on global biosphere productivity

Our hosing-only experiment (Exp_FWF) results in a slowdown of the AMOC from ~17 Sv in the control experiment (Ctrl_40ka) to ~2 Sv. The maximum intensity of AMOC becomes lower than ~4 Sv after 200 years of hosing (Fig. 3). The reorganisation of AMOC leads to a decreased GOP in both the terrestrial- and marine biosphere compared to the control experiment (Fig. 4). Globally, the Exp_FWF experiment yields a GOP of 28.4 ± 0.6 Pmol O_2 $year^{-1}$, or 96 ± 3% of the GOP in Ctrl_40ka simulation (Fig. 8; Table S2).

More specifically, the reduction in land GOP is associated with changes in near-surface temperature and precipitation. Consistent with paleoclimate reconstructions (*e.g., 20*), Exp_FWF experiment exhibits a strong cooling over the North Atlantic and Western

Europe and an overall warming in the Southern Hemisphere. Mean annual precipitation decreases in the northern tropics and increases in the southern tropics, indicating a southward shift of ITCZ in response to abrupt cooling in the Northern Hemisphere (*e.g., 53*). The land GOP is principally limited by temperature and precipitation. As shown by Chen *et al.* (*54*), precipitation (and hence water availability) is the dominant limiting factor for low-latitude GOP, whereas in mid- to high latitude regions, GOP is more likely limited by temperature. As a result, land GOP declines widely across the Northern Hemisphere, particularly in Europe, northernmost South America, northern tropical Africa, and India. This decline is not fully offset by increases in land GOP found in limited regions of the Amazon, South Africa, and northern Australia (Fig. 4).

Marine productivity is primarily limited by nutrient availability. The freshwater hosing suppresses convection and significantly reduces mixed-layer thickness in the North Atlantic Ocean (Fig. 4b). A thinner mixed layer limits the upward transport of nutrients from nutrient-rich deep waters (*26*, *55*) This is directly responsible for the reduction of marine productivity in North Atlantic Ocean. In the Eastern Equatorial Atlantic (Bay of Guinea), the strong decrease in surface ocean nutrient availability and the associated reduction in marine productivity are likely driven by reduced nutrient supply from Antarctic Intermediate Water (AAIW) and Sub-Antarctic Mode Water (SAMW).

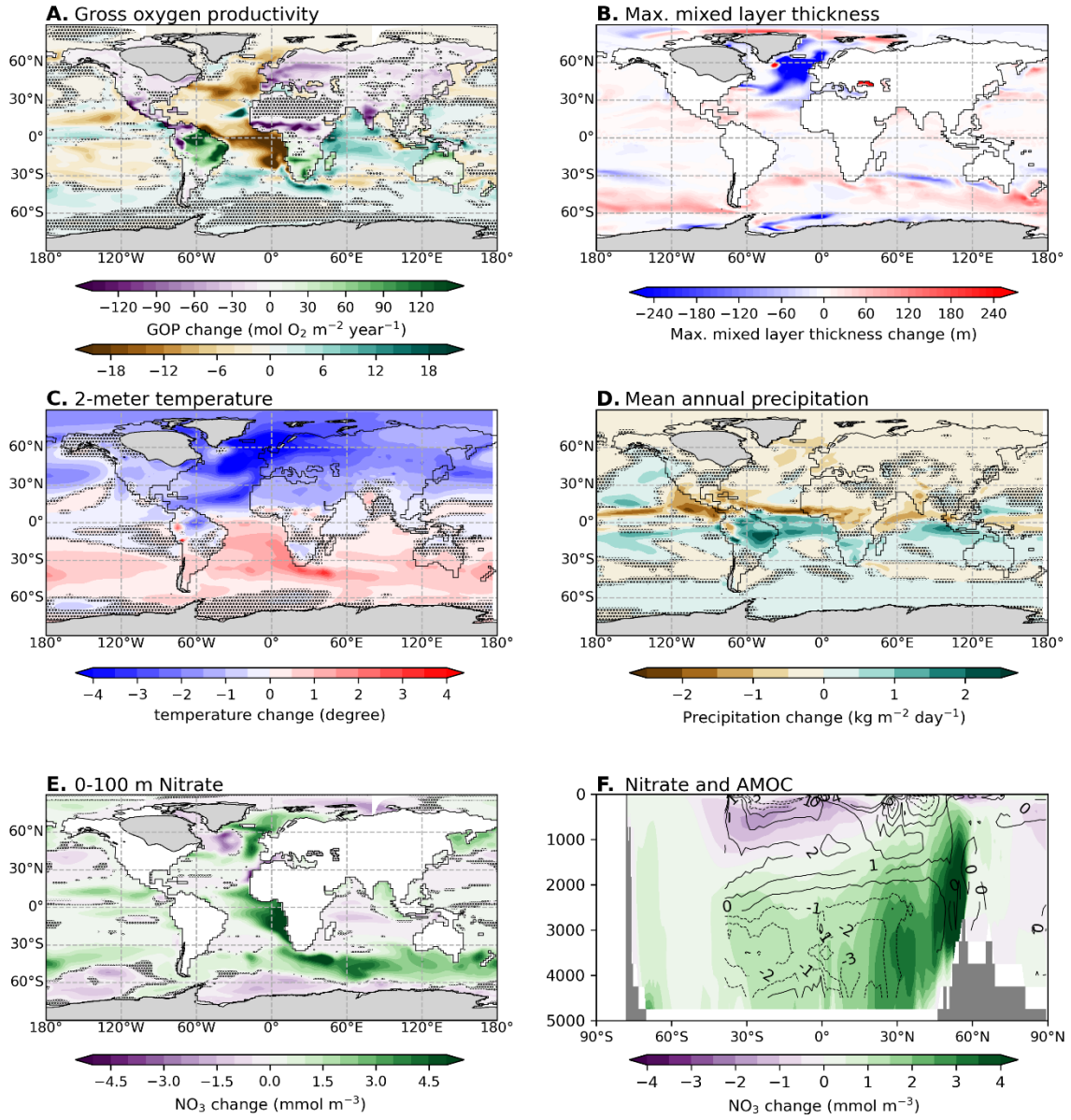

Figure 4. Effects of freshwater hosing in the North Atlantic (Exp_FWF minus Ctrl_40ka). Figures show changes in (**A**) global terrestrial and marine GOP (**B**) maximum mixed layer thickness, (**C**) 2-meter temperature, (**D**) mean annual precipitation, (**E**) surface ocean nitrate concentration, and (**F**) vertical distribution of nitrate concentration in the Atlantic basin. Black contours on (F) indicate zonal mean stream function (in Sverdrup) of Atlantic Ocean in our hosing-only experiment (Exp_FWF). The results are obtained by averaging the last 200 years of integration for both experiments. Where available, stippled regions are not significant at 95% confidence level, according to two-sided Student's t test.

Effect of dust deposition change on marine productivity

Our dust-forcing experiment (Exp_DUST) has a minor effect on the global GOP. This is because the effect of dust deposition is limited to the marine GOP and local changes in marine GOP largely cancel out (Figure 5). As consequence, Exp_DUST experiment leads to an increase in global marine GOP by only 0.1 Pmol O_2 $year^{-1}$ (~1.2% relative to the Exp_FWF simulation), which is insufficient to offset the global GOP decline caused by freshwater hosing (Fig. 8; Table S2)

The H1 dust deposition rate exhibits a strong increase along the Equatorial Pacific and Atlantic, by more than a factor of two in some regions, with an overall increase in the Northern Hemisphere but a significant reduction in the Southern Hemisphere compared to the LGM field (Fig. 5). Accordingly, the simulated marine GOP shows an increase along the Eastern Equatorial Pacific, where the marine productivity is limited by iron. The response of marine GOP is less pronounced in the Equatorial Atlantic (Bay of Guinea) as the marine productivity in this region is less limited by iron. Meanwhile, Exp_DUST experiment shows a significant reduction in marine GOP in the Atlantic sector of the Southern Ocean, where dust deposition strongly declines (Fig. 5). There is a strong simulated increase in GOP in the western coast of South Africa (Southern Benguela coast) despite the overall reduction in dust input in the Southern Hemisphere. This is because the decline in dust-borne iron supply in the Atlantic sector of the Southern Ocean decreases productivity (i.e., decreases nutrient consumption) and enriches the Southern Ocean water masses in other nutrients (e.g., nitrate). Subsequent upwelling of these water masses off eastern South Africa brings nutrient-enriched waters to the surface and enhance productivity.

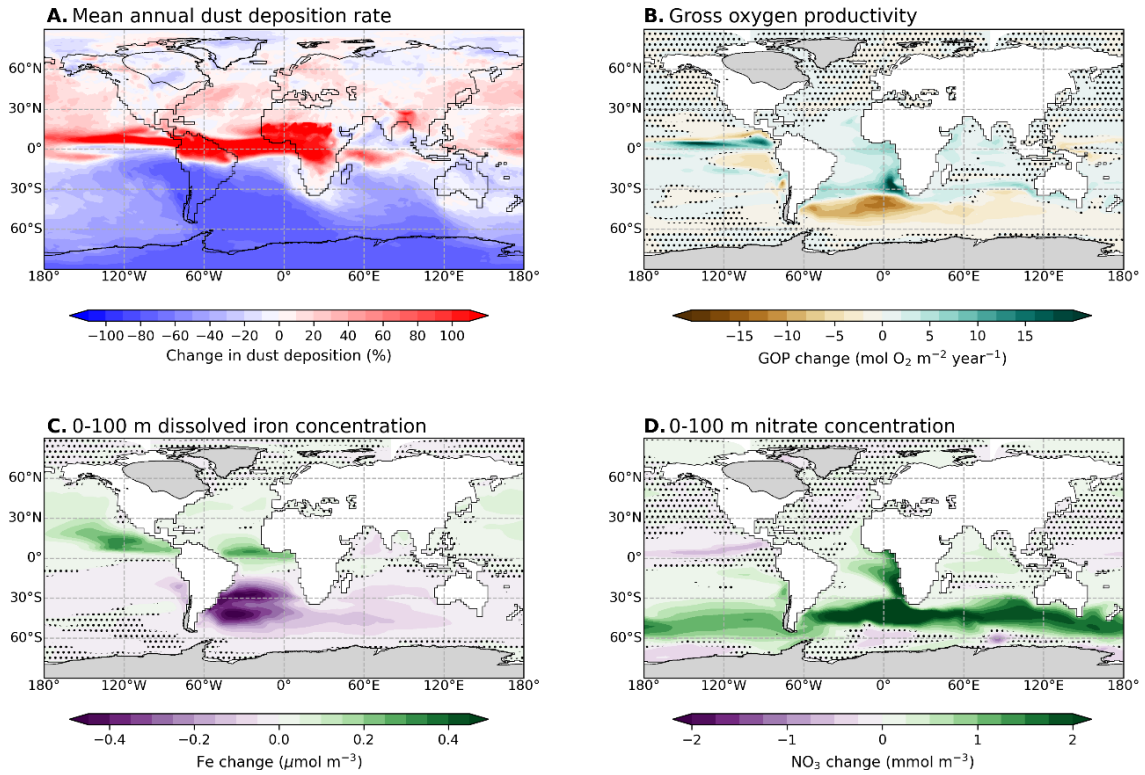

Figure 5. The effects of aeolian dust deposition change on marine productivity (Exp_DUST minus Exp_FWF). (**A**) Mean-annual dust deposition change between 16 ka BP (H1) and 21 ka BP (LGM) scenarios (*56*, *57*). (**B**) Changes in GOP. (**C**) Changes in surface (1 to 100-meter depth) dissolved iron concentration and (**D**) surface nitrate concentration. Terrestrial GOP change is not shown because dust deposition field is only used in PISCES (see text). Where available, stippled regions are not significant at 95% confidence level, according to two-sided Student's t test.

Effects of CO_2 forcing

Our CO_2-forcing experiment (Exp_CO2) results in an enhancement of the global terrestrial GOP by ~0.9 Pmol O_2 year^{-1} (~5.5%) relative to that from Exp_DUST due to the CO_2 fertilization effect and associated climate feedbacks (Fig. 6). In contrast, the CO_2 forcing has negligible influence on marine GOP (Fig. 6) as the phytoplankton growth is not limited by CO_2 (or by inorganic carbon) in the version of PISCES used here (*58*). In total, the CO_2-driven gain in terrestrial GOP induce the simulated global GOP in Exp_CO2 (29.7 Pmol O_2 year^{-1}) close to that of our control simulation (Fig. 8; Table S2).

The increase in land GOP by the prescribed 10-ppm rise in CO_2 concentration mostly occurs in the tropics (between 30°S and 30°N) and the Northern Hemisphere mid-to high latitudes (between 30°N and 90°N), contributing ~0.5 and 0.4 Pmol O_2 year^{-1}, respectively. The respective changes in GOP for tropical (PFTs 2 and 3), temperate (PFTs 4, 5, and 6), and boreal (PFTs 7, 8, and 9) trees are +0.68, +0.20, and +0.26 Pmol O_2 year^{-1}, corresponding to relative changes of +8%, +6%, and +16% compared to Exp_DUST experiment. Our results indicate a stronger sensitivity of boreal trees to CO_2 change compared to tropical and temperate PFTs. This appears inconsistent with the results of

Chen et al. (*54*), where the ORCHIDEE-MICT dynamic global vegetation model is run off-line with prescribed climate and CO_2. The authors found that tropical trees are more sensitive to CO_2 fertilization effect than temperate or boreal type PFTs (*54*). Their results are obtained by single forcing experiments by CO_2 while ours represent comprehensive results including feedbacks by climate and vegetation changes. The pronounced response of boreal forests is also seen in tree fraction change that shows an increase in NH high latitudes vegetation in response to 10 ppm rise of CO_2 (Fig. 6). If the low sensitivity of boreal trees to CO_2 change is held in our model, the seemingly stronger sensitivity to CO_2 in our experiments can be explained by climate effect which is amplified by climate-vegetation feedback. Indeed, Exp_CO2 simulation leads to an increase in mean annual temperature of ~0.5-1°C over most of NH continental high latitudes compared to Exp_DUST (Fig. 6C) as well as an increase in mean annual precipitation in Europe, East Asia, and Africa (Fig. 6d). Therefore, an initial increase in GOP stimulates the growth of boreal forest biomass and hence reduces surface albedo, which in turn increases temperature and further enhances of GPP. Conversely, the limited change in mean annual surface temperature and precipitation, and tree fraction, in the tropics suggest that the GOP in this region is essentially driven by the change in the CO_2 fertilization effect (Fig. 6).

The response of marine GOP to 10 ppm increase in CO_2 in our model is negligible (Fig. 8; Table S2). Temperature changes may alter marine primary productivity but the increase in surface ocean temperatures is small, except in the Arctic and in the highest latitudes of the North Atlantic Ocean (Fig. 6), which are less productive regions because of limited light and nutrient availability.

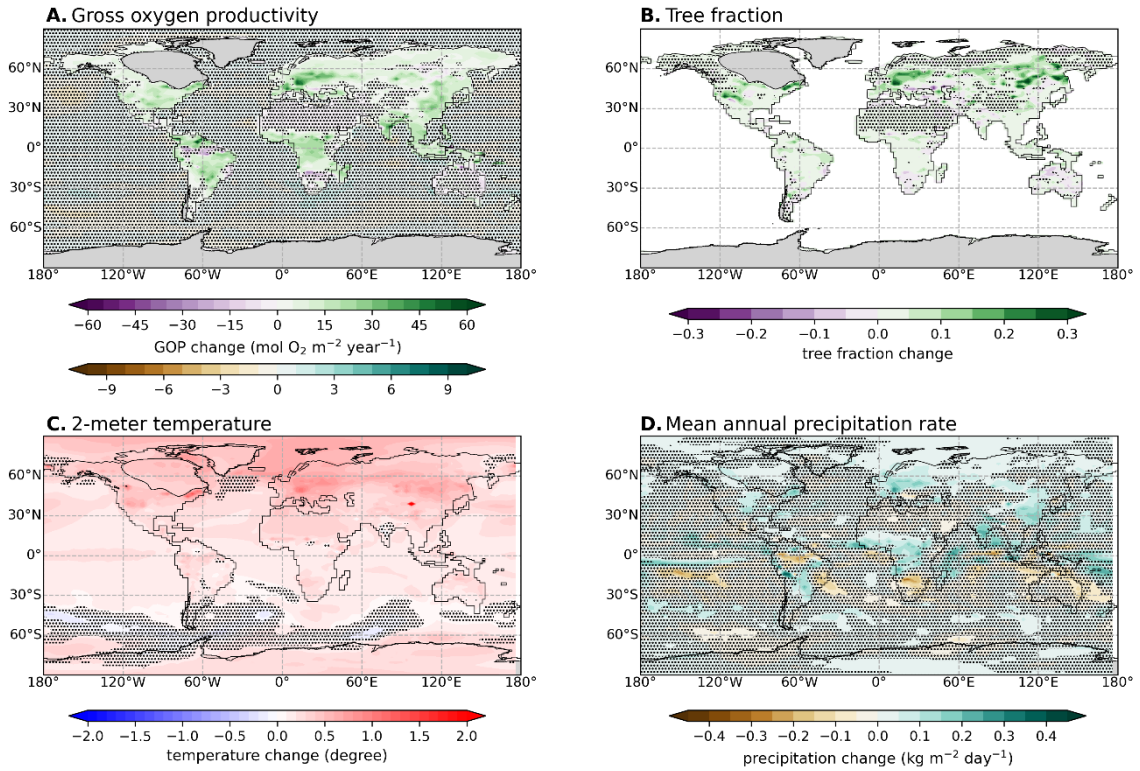

Figure 6. **The effects of CO_2 on global productivity (Exp_CO2 minus Exp_DUST).** (**A**) Changes in global terrestrial and marine biosphere GOP. (**B**) Changes in tree fraction, (**C**) changes in 2-meter temperature, and (**D**) mean annual precipitation rate. Where available, stippled regions are not significant at 95% confidence level, according to two-sided Student's t test.

Effect of dynamic vegetation

Changes in vegetation cover introduce additional feedback mechanisms that can ultimately influence global biosphere productivity. Our fixed vegetation experiment (Exp_VFIX) results in a 0.3 Pmol O_2 $year^{-1}$ (~1.3%) terrestrial GOP increase compared to Exp_CO2. Fixed vegetation simulation demonstrates a slight increase in marine GOP by ~1% compared to that of Exp_CO2, however, the increment in marine GOP (~0.09 Pmol O_2 $year^{-1}$) is of similar order of magnitude as the interannual variability of marine GOP of ~0.11 Pmol O_2 $year^{-1}$ (standard deviation of marine GOP over averaged period), and hence we consider that the effects of vegetation evolution on marine productivity is limited (Fig. 8; Table S2).

The global distribution of GOP changes shows an overall decrease in GOP in SH and increase in NH (Fig. 7). The terrestrial GOP enhancement in NH (0.86 Pmol O_2 $year^{-1}$) outweighs the reduction in the SH (0.62 Pmol O_2 $year^{-1}$). These spatial GOP changes strongly correlate with shifts in tree fraction, highlighting a substantial advance of boreal forests in NH and a retreat of tropical forests at lower latitudes (Fig. 7). The advance of boreal forests at high NH latitudes is associated with additional warming and increased precipitation (Fig. 7).

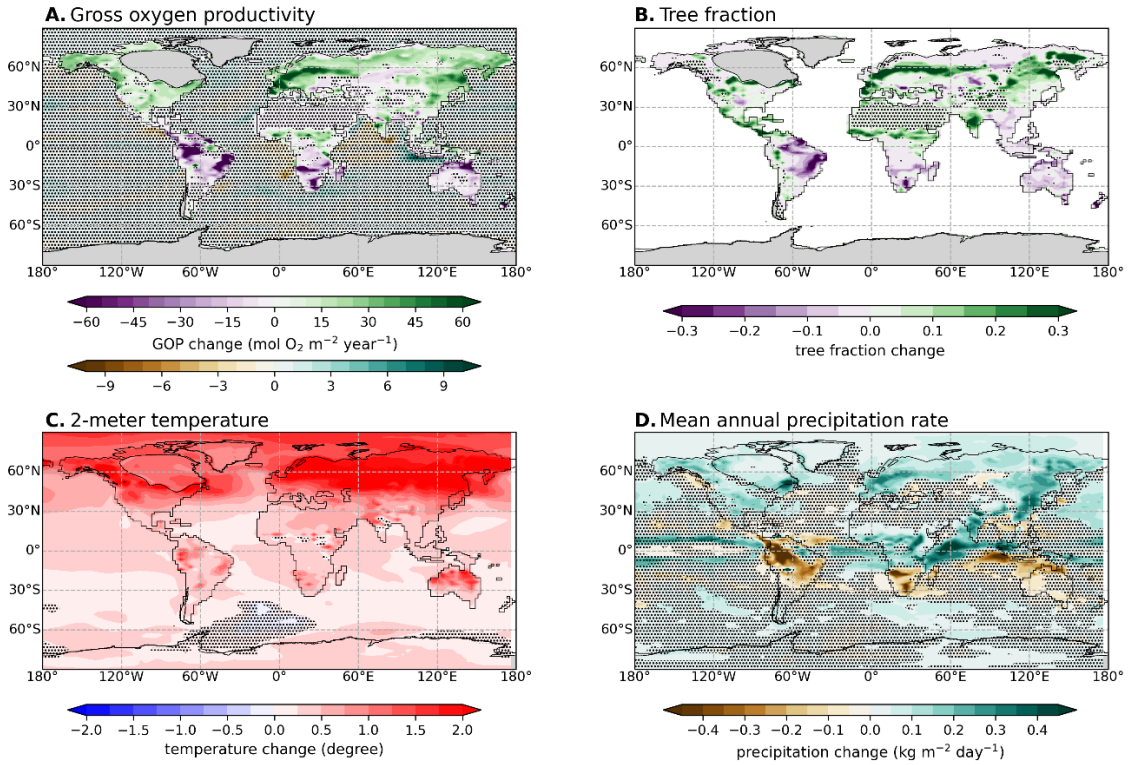

Figure 7. Effects of vegetation change (Exp_VFIX minus Exp_CO2). Same as Figure 5, but for the comparison of Exp_VFIX and Exp_CO2 experiments.

As shown in Figure 7, change in vegetation cover has significant impact on terrestrial GOP, highlighting the importance of the ability of the dynamic global vegetation model (DGVM) to correctly simulate these vegetation changes in response to climate forcing. Comparison with available palynological data shows that our model experiments reasonably capture similar changes in vegetation cover (see Supplementary Material). For instance, in Europe, pollen records demonstrate a retreat of boreal- and temperate forests during Greenland Stadial (GS) 8/9 (HS4) compared to Greenland Interstadial (GI) 8 (*59*). Compared to the vegetation cover in Ctrl_40ka (used in Exp_VFIX), our Exp_CO2 simulation run in DGVM mode results in modelled changes consistent with palynological records: retreat of boreal- and temperate forest in Europe, though grasses are not the dominant biome. The Exp_CO2 experiment also leads to an expansion of bare soil fraction (Fig. S12), although such an increase in the proportion of bare soil cannot be recorded by pollen assemblage data. In addition, this discrepancy in the extent of vegetation change between the pollen data and our model may stem in part from differences in the magnitude of climate forcing between the periods compared—namely, between 40 ka and HS4, and between GI8 and GS8/9.

The comparison of Exp_VFIX and Exp_CO2 hints at the role of vegetation during AMOC reorganization. The initial cooling triggered by AMOC slowdown reduces both GOP and boreal forest extent, leading to increased surface albedo and decreased evapotranspiration—both of which further suppress GOP. Similarly, the expansion of tropical and temperate forests in the Amazon and South Africa corresponds to regions of higher mean annual precipitation, potentially enhancing vegetation GOP.

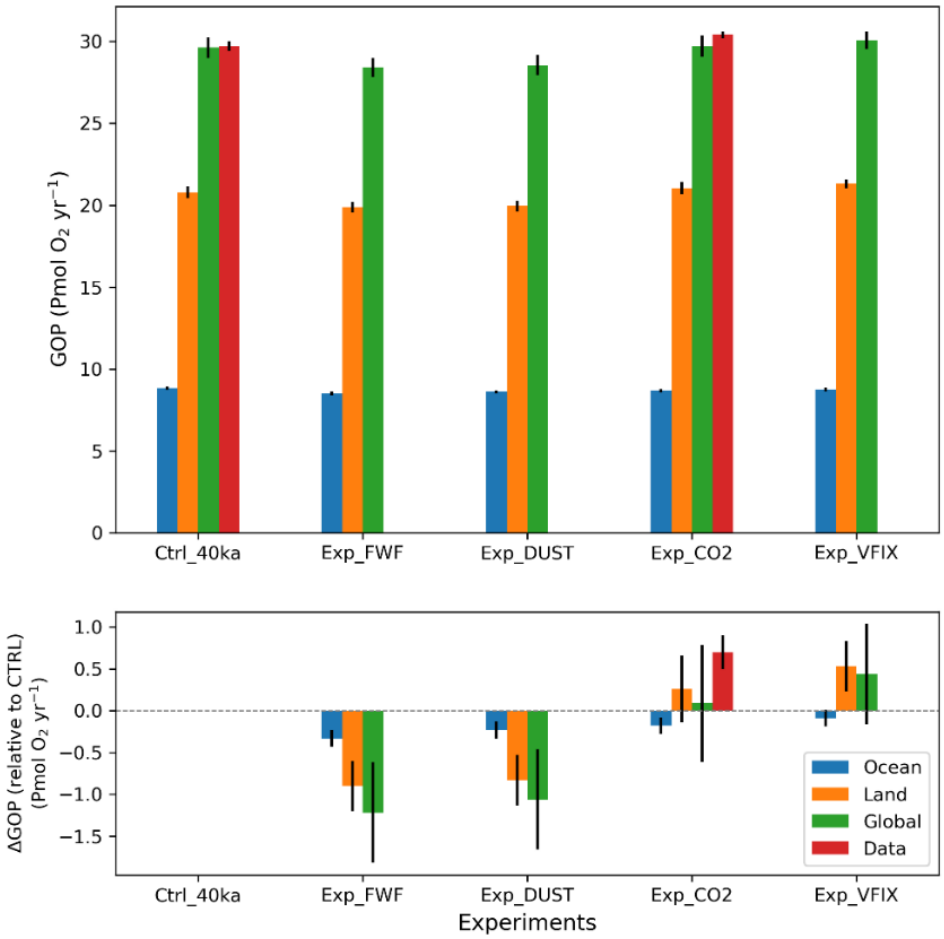

Figure 8. **Comparison of GOP obtained in this study.** *Upper panel*: The marine (blue), terrestrial (orange) and global (green) GOP obtained in GCM experiments, compared with results from ice-core $^{17}\Delta$ data (red) for Periods I (corresponds to Ctrl_40ka) and II (Exp_CO2). The black error bars represent the 1-sigma variation of model outputs over the integrated period. The GOP values from ice-core data are calculated by multiplying the preindustrial GOP obtained from IPSL-CM5A2-VLR experiments. *Bottom panel*: Identical to upper panel but shows differences relative to Ctrl_40ka experiments.

Discussion

In this paper, we present a new $^{17}\Delta$ record from the NEEM ice core covering the HS4 interval. The new $^{17}\Delta$ records and box model experiments point to an increase in GOP following the abrupt CO_2 jump at ~39.5ka BP (in WD2014 age scale). Our GCM experiments of the idealized Heinrich-like forcing (hosing + dust + CO_2 + dynamic vegetation) demonstrate a non-significant change in GOP, contrary to previous studies.

Past modeling studies have suggested a decline in GOP in their idealized Heinrich-like GCM experiments, as the AMOC collapse leads to NH cooling and drying, along with ocean circulation changes that reduce terrestrial (*28*) and marine (*26*) productivity. We observe similar results in our freshwater hosing-only experiment (Exp_FWF), suggesting that the physical consequences (*i.e.,* cooling and drying of the NH and warming and moistening of the SH) of a collapse of the AMOC on global biosphere production is

robust. However, the inclusion in the model of additional climatic and environmental changes documented in the proxy record across HS, in particular the atmospheric CO_2 concentration and aeolian dust inputs, allows counterbalance the GOP decline resulting from the collapse of the AMOC (Exp_CO2 experiment). In particular, the fertilization effect and the modest warming associated with the imposed CO_2 increase stimulate terrestrial productivity, thereby allowing global biosphere productivity to rebound to a level similar (within uncertainties) to that of the Ctrl_40ka experiment. Although our new $^{17}\Delta$ measurements indicate an increase in GOP, the findings from our GCM simulations are encouraging as they provide potential feedback mechanisms for compensating the effects of AMOC weakening on global biosphere productivity.

Interestingly, promising avenues for improvement exist to better reconcile the results obtained from the ice-core $^{17}\Delta$ record and our numerical experiments using IPSL-CM5A2-VLR GCM. First, in our simulations, we prescribed a constant freshwater flux of 0.2Sv, which results in an almost complete collapse of the AMOC. Recent work instead suggests that the AMOC may have survived in a state of intermediate intensity during HS (*60*). This may reduce the magnitude of GOP decrease driven by the HS4 climate perturbation and, combined with the effects of CO_2 and dust, enhance global productivity in our HS4-like experiments. Second, and contrary to the marine productivity, the terrestrial productivity does not rely on nutrient supply in our vegetation model. This means that any changes in aeolian nutrient supply over continental areas do not impact the simulated terrestrial GOP. Heinrich-like simulations exhibit large changes in dust supply (*e.g., 57*) (Figure 5), in particular more than a doubling over tropical Africa and Amazonia, which correspond to highly productive regions. We can speculate that this could have stimulated productivity in these regions during HS4, and note that this could be investigated with more recent versions of ORCHIDEE model, which incorporate representations of the aeolian deposition of nutrients (*e.g., 61, 62*). Third, our Exp_CO2 simulation underlines the impact of a prescribed CO_2 rise of 10 ppmv on global biosphere productivity. As ice-core records from WAIS Divide indicate a 13 ppmv rise of CO_2 between the average over Period I and Period II (*25*), we can speculate that this would further enhance terrestrial productivity. Fourth, biogeochemical feedbacks affecting marine productivity could be better integrated and might affect the global productivity. In our simulations, the riverine inputs in nutrients are fixed in time (but the freshwater runoff freely evolves with climatic conditions) and therefore do not reflect changes in precipitation patterns although this could influence marine productivity in coastal regions. In addition, phytoplankton growth is not limited by dissolved inorganic carbon in in PISCES, despite some laboratory culture experiments reporting fertilization effects from inorganic carbon or CO_2 (*63*, *64*). However, the effect of these processes on global marine productivity are harder to grasp. Addressing above mentioned limitations may allow to better reconcile the GOP reconstruction from the ice-core $^{17}\Delta$ records and GCM experiments.

Ideally, the interpretation of ice-core $^{17}\Delta$ records could be improved through the use of a water and O_2 isotope-enabled Earth System Model (ESM) and/or a coupled climate-chemistry model. An oxygen isotope-enabled ESM would better capture the spatial variability of isotopic ratio of source water associated with meridional shifts of ITCZ, changes in isotope fractionation linked to vegetation dynamics, or the influence on the isotopic composition of dissolved O_2 in the ocean by dynamical processes. Meanwhile, a climate-chemistry model could explicitly assess the sensitivity of the stratospheric isotopic effect to CO_2 (presumed to be linearly correlated in this study) and other potential perturbations of the stratosphere, such as the Laschamp Excursion, which occur just

before HS4 and may have significantly influence the stratospheric chemistry (*65*) and hence the oxygen isotope fractionation of O_2. These advances however would require substantial future model development work.

Our interpretation of ice-core $^{17}\Delta$ records is consistent with the hypothesis of rapid vegetation regrowth following the extended biomass burning (*24*). This hypothesis is proposed by experiments with a carbon-cycle box model (*23*) incorporating the abrupt terrestrial carbon release by biomass burning, that require an enhanced net primary productivity to stabilize CO_2 and $\delta^{13}C$-CO_2 following the abrupt rise (*24*). Our results thus provide an independent evidence for the increase in global terrestrial biosphere productivity during this interval. The extended biomass burning may result in a sharp decline in GOP at ~39.5 ka BP followed by a rapid increase over a few hundreds of years. However, temporal resolution of current data set does not allow to properly resolve these even finer-scale temporal variations. Higher-precision, sub-centennial-scale measurements of $^{17}\Delta$ will be necessary to capture sub-millennial changes during HS4, as indicated by various paleoclimatic proxy records from this interval (*e.g., 44, 66*).

Overall, from our new ice-core measurements of $^{17}\Delta$ from NEEM ice core and climate model experiments, we conclude that GOP more likely increases during HS4, following the abrupt CO_2 jump at 39.5 ka BP. Although our GCM simulations do not show a clear increase in global GOP, we demonstrate that the abrupt CO_2 emission and its fertilization effect offsets the decline in biosphere productivity caused by abrupt climate change associated with AMOC slowdown.

If future AMOC perturbation occurs alongside abrupt CO_2 emission – either via deep ocean ventilation or enhanced biomass burning – the global biosphere will likely contribute to dampen the CO_2 rise. To better understand this potential feedback, a dedicated study combining $\delta^{13}C$-CO_2 and $^{17}\Delta$ would be valuable in shedding light on interactions between biosphere productivity and change in carbon reservoirs.

Materials and Methods

Triple oxygen isotope analysis of air O_2 from ice-core samples

We measured the $\delta^{17}O$ and $\delta^{18}O$ of air O_2 enclosed in the North Greenland Eemian Ice Drilling (NEEM) ice-core samples over 36.7 to 42.1 ka BP interval. The ice-core measurements were made at Laboratoire des Sciences du Climat et de l'Environnement (LSCE, Saclay, France) using the semi-automated gas extraction and purification system similar to that described in Barkan and Luz (*67*). In brief, about ~20 g of ice samples is melted in pre-evacuated glass flasks submerged in a tap water bath at ambient temperature (20ºC) for 40 minutes. The extracted air is passed through a H_2O (liquid nitrogen) and CO_2 trap (liquid N_2 and ethanol mixture), and then is gas chromatographed below at 0ºC to separate O_2 and Ar from N_2. The O_2-Ar mixture is cryogenically trapped by stainless steel tubes submerged in liquid helium reservoir. The samples tubes rest in ambient temperature for ~3 hours for untrapping and homogenization before injection to Thermo Finnigan MAT 253 isotope-ratio mass spectrometer.

The $^{17}\Delta$ data have been corrected for gravitational enrichment, pore close-off, and gas loss during sample storage. The gravitational settling effect in the firn column is corrected using published NEEM $\delta^{15}N$-N_2 data (*44*). The correction for pore close-off is in the order of 13 ppm, based on the $^{17}\Delta$ measurements from the firn-ice transition zone at the NEEM drilling site (*35*). The gas-loss effect has been quantified by parallel analysis of O_2-Ar ratio (*35*, *36*).

The standard of choice is contemporary air collected in Saclay, France, whose triple isotopic composition of O_2 and molecular ratio of O_2 to Ar are determined by regular measurements. The contemporary air is collected in early morning at each day of ice-core measurements. At least two contemporary air samples are measured to trace daily blank effect and bias among the different sample tubes. The first sample is used for priming the gas purification line and whose result is not used in our analysis. Daily measurements of modern air allow us to trace daily variations of blank effect of the extraction system.

Synchronization of the ice-core records to the WD2014 time scale

We synchronize the ice-core records used in the analysis to the WAIS-Divide age scale (WD2014). The NEEM $\delta^{18}O_{atm}$ and $^{17}\Delta$ data are transferred to WD2014 time scale by matching the continuous CH_4 records from both drilling sites (*40*, *41*). The Siple Dome $\delta^{18}O_{atm}$ record is synchronized to the NEEM CH_4 record on WD2014 time scale using the tie points determined by Guillevic *et al*. (*44*). The NGRIP water isotope record is transferred to WD2014 scale by multiplying a constant factor of 1.0063 to its original age following Buizert *et al*. (*68*).

The $^{17}\Delta$ box model

We use the box model of triple isotope composition of O_2 developed by Blunier *et al*. (*33*), which accounts for major fluxes and fractionation effects of O_2 in the biosphere, hydrosphere, and stratosphere. The time derivative of the mass of $^{33}O_2$ ($^{17}O^{16}O$) and $^{34}O_2$ ($^{18}O^{16}O$) are given as follows:

$$\frac{\mathrm{d}}{\mathrm{dt}}(M\ {}^{x}R_{atm}) = F_{op}\ {}^{x}\alpha_{op}\ {}^{x}R_{sw} - F_{or}\ {}^{x}\alpha_{or}\ {}^{x}R_{atm} + F_{lp}\ {}^{x}\alpha_{lp}\ {}^{x}R_{sw} - F_{lr}\ {}^{x}\alpha_{lr}\ {}^{x}R_{atm} + F_{str}\ {}^{x}\alpha_{str}\ {}^{x}R_{atm} - F_{str}\ {}^{x}R_{atm} \quad (1)$$

where superscript x indicates rare oxygen isotopes of 17 and 18, M the mass of troposphere, ${}^{x}R$ the isotopic ratio, F the oxygen flux, and alpha the isotopic fractionation factor. To calculate total masses of rare isotopologues we assume that the masses of rare isotopologues are negligible so that $M\frac{^{18}O}{^{16}O} = M\frac{^{18}O}{O_2}$. The subscript of o and l represents ocean and land processes, and p and r the photosynthesis and respiration, and atm, sw, and str the troposphere, seawater, and the stratosphere respectively. We assume that M is constant and isotopic ratios of air O_2 are in steady state (i.e., $\frac{\mathrm{d}}{\mathrm{dt}}(M\ {}^{x}R_{atm}) \approx 0$). The latter one is justified by relatively long atmospheric lifetime of O_2 (e.g., Bender et al., 1994).

The above system is underconstrained, with 6 unknowns (F_{op}, F_{lp}, F_{or}, F_{lr}, h, α_{str}) but only two equations for $^{33}O_2$ and $^{34}O_2$. To reduce the number of unknowns, we assume that the terrestrial and ocean biospheres are at equilibrium (i.e., F_{op}=F_{or} and F_{lp}=F_{lr}). We determine the pre-industrial h and α_{str} values during the model initialization using pre-industrial boundary conditions (i.e., $\delta^{18}O_{atm}$ = 0‰, $^{17}\Delta$ = 0 ppm, F_{lp} = 2.43 Pmol year^{-1} and F_{op} = 1.08 Pmol year^{-1}). To calculate the past variations of α_{str}, we assume that $^{18}\varepsilon_{str}$= $^{18}\alpha_{str}$ −1 varies proportionally with atmospheric CO_2, based on the fact that CO_2 plays important role in depleting heavy oxygen isotopes in O_2 (*47*). The h is kept constant in our model experiments.

The isotopic composition of leaf water (α_{lp}) is calculated using the following formulation (*70*):

$$\alpha_{lp} = [\alpha_S \alpha_k (1-h) + \alpha_V h]\alpha_{eq} \quad (2)$$

where α_k and α_{eq} are the kinetic and equilibrium fractionation factors, and h indicates the relative humidity. The α_S and α_V are the isotopic composition of (GPP-weighted) precipitation water and (GPP-weighted) water vapor, respectively, expressed in fractionation factor relative to R_{sw}. The values of these fractionation factors are adopted from Blunier *et al*. (*33*).

The terrestrial respiratory fractionation factor (α_{lr}) is calculated as a weighted average of isotope fractionation during O_2 consumption via dark respiration in soil and in leaves, photorespiration, Mehler reaction and respiration via alternative oxidase. The values of these fractionation factors are taken from Blunier *et al.* (*33*). The fraction of photorespiration is calculated as the fraction of C4 photosynthesis as we assume no photorespiration in C4-type vegetation. The fraction of C4 photosynthesis is inversely scaled to the CO_2 concentrations between 0.275 (PI) and 0.39 (LGM) following Blunier *et al.* (*33*). The fraction of respiration via Mehler reaction and alternative oxidase are assumed to be constant at 10 and 2%, respectively.

The marine photosynthetic fractionation factor (α_{op}) and the ln(δ^{17}O+1)/ln(δ^{18}O+1) slope ($\theta^{17/18}$) are prescribed to be 1.004 and 0.524 respectively. These values are obtained from the biological chamber experiments using different phytoplankton species (*69* and references therein). The marine respiratory fractionation factor (α_{or}) and the associated $\theta^{17/18}$ is taken as 0.9785 and 0.518, respectively. The α_{or} value is obtained by weighted

average of respiratory fractionation factor in the surface ocean ($\alpha_{ors} = 0.978$) and that in the deep ocean ($\alpha_{ord} = 0.988$). The fraction of marine respiration in the surface ocean is assumed to be 95% of the total respiration.

Following Blunier *et al.* (*33*), we prescribe the land productivity (F_{lp}) using a polynomial regression curve relating GPP (in carbon) to CO_2 from the transient simulation of LPJ-DGVM (*71*). The modeled GPP is converted to GOP using the relationship between the actual electron transport rate and the CO_2 assimilation rate (*72*), following Eq. (4) of Blunier *et al*. (*33*).

Given the prescribed land productivity, the ocean productivity (F_{op}) can be calculated using the Equation 1:

$$F_{op} = F_{lp}\left[\frac{{}^{x}\alpha_{lp}\,{}^{x}R_{sw} - {}^{x}\alpha_{lr}\,{}^{x}R_{atm}}{{}^{x}\alpha_{or}\,{}^{x}R_{atm} - {}^{x}\alpha_{op}\,{}^{x}R_{sw}}\right] + \frac{F_{str}\,{}^{x}R_{atm}\left({}^{x}\alpha_{str} - 1\right)}{{}^{x}\alpha_{or}\,{}^{x}R_{atm} - {}^{x}\alpha_{op}\,{}^{x}R_{sw}} \quad (3)$$

where the superscript x denotes the rare oxygen isotopes, 17 or 18. The global productivity is then calculated as the sum of land and ocean productivity.

The input data for the $^{17}\Delta$ box model are taken from ice-core measurements and the published literature. For $\delta^{18}O_{atm}$, we use measurements from the NEEM ice core (*44*). CO_2 records are from the WAIS Divide ice core on its WD2014 time scale (*25*). For $\delta^{18}O$ of seawater ($\delta^{18}O_{sw}$), we scaled the absolutely dated relative sea-level reconstruction data from Red Sea (*73*) to 0 (modern) to 1‰ (LGM) to obtain high-resolution $\delta^{18}O_{sw}$ record. All the data are linearly interpolated to each time step of $^{17}\Delta$ data. The $^{17}\Delta$ and $\delta^{18}O_{atm}$ data from NEEM ice core were transferred to WD2014 time scale by CH_4 correlation.

We obtain the modeled $^{17}\Delta$ and $\delta^{18}O_{atm}$ curves (Fig. 2) using following equation derived by rearranging Equation 1:

$${}^{x}R_{atm} = \frac{F_{op}\,{}^{x}\alpha_{op}\,{}^{x}R_{sw} + F_{lp}\,{}^{x}\alpha_{lp}\,{}^{x}R_{sw}}{F_{or}\,{}^{x}\alpha_{or} + F_{lr}\,{}^{x}\alpha_{lr} + (1 - {}^{x}\alpha_{str})F_{str}} \quad (4)$$

where superscript x represents 17 and 18, and we assume F_{op}=F_{or} and F_{lp}=F_{lr}. The CO_2-effect-only scenario is calculated by prescribing biosphere fluxes (F_{lp}, F_{op}), fractionation factors (α_{lp}, α_{lr}, α_{op}, α_{or}), and water isotopic ratios (R_{sw}) to the values of Period I.

Global climate model experiments

The IPSL-CM5A2-VLR Earth System Model (described and evaluated in Sepulchre et al., 2020) is composed of the LMDZ atmosphere model (*74*), the ORCHIDEE land surface and vegetation model (*75*), and the NEMO ocean model (*76*). NEMO (version 3.6) itself consists of the OPA dynamic ocean model, the LIM2 sea-ice model (*77*) and the PISCES-v2 marine biogeochemistry model (*58*). OASIS (*78*) is used to couple the models, and XIOS (*79*) handles input/output processing. LMDZ and ORCHIDEE share the same horizontal resolution of 3.75° × 1.875° (longitude × latitude) and LMDZ is discretized into 39 uneven levels in the vertical. NEMO has a nominal horizontal resolution of 2°, enhanced to 0.5° at the equator, and 31 vertical levels whose thickness varies from 10 m at the surface to 500 m at the bottom. NEMO uses a tripolar grid to overcome the North Pole singularity (*80*). This version of the IPSL model is essentially a re-tuned version of the

IPSL-CM5A model (*81*) with reduced biases and better numerical performances (*37*). It has been applied extensively in the past years to simulate modern (*e.g., 82*) and past climates (*e.g., 83*), including Quaternary climates (*e.g., 84*).

Here, we design new experiments to simulate the effects of the HS4 perturbation on the global biosphere productivity. Our control experiment features boundary conditions for 40ka BP to provide a reference global biosphere productivity just before the onset of HS4. To this end, we used the 40ka land-sea mask and ice-sheet topography provided by the recent reconstruction of Gowan *et al*. (*85*). This new ice-sheet reconstruction is characterized by a smaller ice-sheet extent and hence higher global sea level compared to the 16ka ice-sheet geometry that was used as an analogue of MIS3 and MIS4 ice sheets in previous model simulations (*e.g., 86*). Other important boundary conditions for the control experiment include an atmospheric CO_2, CH_4, and N_2O concentrations of 200 ppmv, 450 ppbv, and 240 ppbv, respectively, and the LGM dust deposition created by Albani *et al*. (*56*). The control simulation is run for 1100 years from the end of the previous MIS3 simulation under 46ka boundary condition (*87*). A brief evaluation of the mean climate state of this new 40ka simulation and its comparison to a reference IPSL-CM5A2-VLR preindustrial simulation of this new 40ka simulation is presented in the next section.

From our control simulation, we branch four 400-year perturbation experiments that are designed to investigate the effect of a Heinrich event on different known drivers of biosphere productivity changes. To this end, we sequentially cumulate the drivers affected by a Heinrich-like state: in the first experiment (Exp_FWF), a constant, uniformly-distributed freshwater flux of 0.2 Sv is added to the North Atlantic Ocean between 40°N and 80°N for a duration of 400 years to perturb the AMOC. In the second experiment (Exp_DUST), besides the same freshwater flux, we impose the H1 (16 ka BP) dust deposition field (*56*, *57*) instead of the LGM (21 ka BP) one (*56*, *57*). The difference between Exp_DUST and Exp_FWF therefore indicate the influence of dust deposition change on the global GOP. The third experiment (Exp_CO2) adds the effect of a slightly increased atmospheric CO_2 (to 210 ppmv), mimicking the CO_2 increase documented in the ice core record of Wendt *et al*. (*25*) across HS4. The difference between Exp_CO2 and Exp_DUST represents the effect of CO_2 rise. Finally, in order to examine the effect of vegetation dynamics, the last experiment (Exp_VFIX) is set to identical to Exp_CO2 but the vegetation cover is fixed to that obtained at the end of the control (Ctrl_40ka) simulation. Results presented and discussed in the manuscript are the climatological average of years 201-400, unless otherwise specified.

In each simulation, terrestrial GOP is calculated directly by ORCHIDEE land surface model. We assume that GOP equals to the flux of O_2 produced at Photosystem II by splitting water molecules, before partially consumed by photorespiration during PCO cycle (*72*). Resulting GOP values show a near-linear relationship with gross primary carbon productivity (GPPC) with a slope of ~2 (Fig. 3). The GOP-GPPC slope is insensitive to latitudes. The slope is greater than the typical value of photosynthetic quotient of ~1.1 (moles O_2) (moles C)$^{-1}$. The GOP-GPPC difference reflects the photorespiratory O_2 consumption. Marine GOP is calculated using the new and regenerated primary productivity obtained in PISCES marine biogeochemistry model by multiplying photosynthetic quotient and a factor of 2.3 to convert to GOP.

40ka mean climate state

Surface diagnostics of the 40ka simulation are presented in Fig. S4. The mean annual 2-meter temperature (T2m) varies from lower than 214 to greater than 297°C, over the interior east Antarctica and the tropical regions respectively. Globally averaged T2m in our Ctrl_40ka is 282.9±0.1°C, which is 3.4±0.1°C cooler than that obtained from PREIND experiment, and thereby lying between the global mean surface temperature (GMST) of the LGM and the PI. This is expected as the prescribed CO_2 concentration and ice sheet cover are intermediate states between those of the LGM and the PI. Accordingly, regions of largest temperature differences in our 40ka simulation compared to the PI are those that become covered by perennial ice sheets (northern North America), as is the case in the PMIP4 LGM-PI temperature difference (*84*).

The Ctrl_40ka experiment also results in a drier climate compared to PREIND, despite increase in precipitation rate is observed in several regions (Fig. S7). The precipitation patterns in our Ctrl_40ka are also similar to the LGM (*84*) with an overall decrease in the high latitudes and the equatorial band (amplified over Indonesia) compared to PREIND (Fig. S7) (*84*). The global mean yearly total (liquid + solid) precipitation rate is reduced by 0.22±0.01 kg m^{-2} day^{-1} (Fig. S4).

The globally-averaged simulated global biosphere productivity (GOP) in Ctrl_40ka is 85% of that obtained in PREIND experiment. As expected from the large decrease in prescribed atmospheric CO_2 and cooler and drier climate in Ctrl_40ka simulation, the terrestrial productivity declines substantially compared to PI (85% compared to PREIND; Fig. S7). The decrease in terrestrial GOP occurs in NH high latitudes and tropical regions, where the model predicts significant cooling and/or drying (Fig. S7). The marine productivity (82% compared to PREIND) exhibits an overall decline between 30°S and 30°N but increases in the Atlantic and Indian sectors of the Southern Ocean as well as in the North Atlantic and North Pacific gyres. In the low latitudes, the decrease in productivity is likely linked to reduced low-latitude upwelling under colder climates (e.g., *88*). In the northern high latitudes, productivity increases in the North Atlantic because of the increased AMOC intensity and penetration depth in our Ctrl_40ka simulation compared to PI (Fig. S7). These two characteristics of the AMOC are a known consequence of glacial climate forcing in many ESMs, in particular IPSL-CM5A (*84*). In our Ctrl_40ka simulation, the more vigorous and deeper AMOC (Fig. S8) is associated with deeper mixed-layer depth which increases the vertical mixing of the upper ocean and remobilizes subsurface nutrients, enhancing productivity there. In the Atlantic and Indian sectors of the Southern Ocean, the large increase in dust deposition prescribed in Ctrl_40ka simulation is likely the dominant driver of the increased productivity in these iron-limited zones (*88*). Overall, the simulated 40ka climate resembles an intermediate state between the full LGM climate conditions and the PI.

References

1. P. G. Falkowski, J. A. Raven, *Aquatic photosynthesis*. (Princeton University Press, 2013).
2. T. F. Keenan, X. Luo, B. D. Stocker, M. G. De Kauwe, B. E. Medlyn, I. C. Prentice, N. G. Smith, C. Terrer, H. Wang, Y. Zhang, S. Zhou, A constraint on historic growth in global photosynthesis due to rising CO_2. *Nat. Clim. Change* **13**, 1376-1381 (2023).
3. A. U. Igamberdiev, P. J. Lea, Land plants equilibrate O_2 and CO_2 concentrations in the atmosphere. *Photosynth. Res*. **87**, 177-197 (2006).
4. H. D. Holland, The oxygenation of the atmosphere and oceans. *Philos. Trans. R. Soc. B, Biol. Sci.* **361**, 903-915 (2006).
5. C. B. Field, M. J. Behrenfeld, J. T. Randerson, P. Falkowski, Primary production of the biosphere: Integrating terrestrial and oceanic components. *Science* **281**, 237-240 (1998).
6. C. Beer, M. Reichstein, E. Tomelleri, P. Ciais, M. Jung, N. Carvalhais, C. Rödenbeck, M. Altaf Arain, D. Baldocchi, G. B. Bonan, A. Bondeau, A. Cescatti, G. Lasslop, A. Lnndroth, M. Lomas, S. Luyssaert, H. Margolis, K. W. Oleson, O. Roupsard, E. Veenendaal, N. Viovy, C. Williams, F. Ian Woodward, D. Papale, Terrestrial gross carbon dioxide uptake: Global distribution and covariation with climate. *Science* **329**, 834-838 (2010).
7. A. Anav, P. Friedlingstein, C. Beer, P. Ciais, A. Harper, C. Jones, G. Murray-Tortarolo, D. Papale, N. C. Parazoo, P. Peylin, S. Piao, S. Sitch, N. Viovy, A. Wiltshire, M. Zhao, Spatiotemporal patterns of terrestrial gross primary production: A review. *Rev. Geophys*. **53**, 785-818 (2015).
8. S. Rahmstorf, J. E. Box, G. Feulner, M. E. Mann, A. Robinson, S. Rutherford, E. J. Schaffernicht, Exceptional twentieth-century slowdown in Atlantic Ocean overturning circulation. *Nat. Clim. Change* **5**, 475-480 (2015).
9. P. Ditlevsen, S. Ditlevsen, Warning of a forthcoming collapse of the Atlantic meridional overturning circulation. *Nat. Commun*. **14**, 4254 (2023).
10. M. Kageyama, U. Merkel, B. Otto-Bliesner, M. Prange, A. Abe-Ouchi, G. Lohmann, R. Ohgaito, D. M. Roche, J. Singarayer, D. Swingedouw, X. Zhang, Climatic impacts of fresh water hosing under Last Glacial Maximum conditions: a multi-model study. *Clim. Past* **9**, 935-953 (2013).
11. L. C. Jackson, R. Kahana, T. Graham, M. A. Ringer, T. Woollings, J. V. Mecking, R. A. Wood, Global and European climate impacts of a slowdown of the AMOC in a high resolution GCM. *Clim. Dyn*. **45**, 3299-3316 (2015).
12. W. Liu, A. V. Fedorov, S.-P. Xie, S. Hu, Climate impacts of a weakened Atlantic Meridional Overturning Circulation in a warming climate. *Sci. Adv*. **6**, eaaz4876 (2020).
13. B. Fox-Kemper, H. T. Hewitt, C. Xiao, G. Aðalgeirsdóttir, S. S. Drijfhout, T. L. Edwards, N. R. Golledge, M. Hemer, R. E. Kopp, G. Krinner, A. Mix, D. Notz, S. Nowicki, I. S. Nurhati, L. Ruiz, J.-B. Sallée, A. B. A. Slangen, Y. Yu, Ocean, cryosphere, and sea level change, in *Climate Change 2021: The Physical Science Basis. Contribution of Working Group I to the Sixth Assessment Report of the Intergovernmental Panel on Climate Change* (Cambridge Univ. Press, 2021), chap. 9.
14. R. Liebermann, M. Hofmann, G. Feulner, Shutdown of Atlantic overturning circulation could cause persistent increase of primary production in the Pacific. *Environ. Res. Lett*. **19** 024005 (2024).
15. W. Dansgaard, S. J. Johnsen, H. B. Clausen, D. Dahl-Jensen, N. S. Gunderstrup, C. U. Hammer, C. S. Hvidberg, J. P. Steffensen, A. E. Sveinbjörnsdottir, J. Jouzel, G. Bond, Evidence for general instability of past climate from a 250-kyr ice-core record. *Nature* **364**, 218-220 (1993).

16. T. Blunier, E. J. Brook, Timing of millennial-scale climate change in Antarctica and Greenland during the last glacial period. *Science* **291**, 109-112 (2001).
17. WAIS Divide Project Members, Precise interpolar phasing of abrupt climate change during the last ice age, *Nature* **520**, 661-665 (2015).
18. T. F. Stocker, S. J. Johnsen, A minimum thermodynamic model for the bipolar seesaw, *Paleoceanography* **18**, 1087 (2003).
19. J. B. Pedro, M. Jochum, C. Buizert, F. He, S. Barker, S. O. Rasmussen, Beyond the bipolar seesaw: Toward a process understanding of interhemispheric coupling. *Quat. Sci. Rev*. **192**, 27-46 (2018).
20. S. Barker, P. Diz, M. J. Vautravers, J. Pike, G. Knorr, I. R. Hall, W. S. Broecker, Interhemispheric Atlantic seesaw response during the last deglaciation. *Nature* **457**, 1097-1102 (2009).
21. L. G. Henry, J. F. McManus, W. B. Curry, N. L. Roberts, A. M. Piotrowski, L. D. Keigwin, North Atlantic ocean circulation and abrupt climate change during the last deglaciation. *Science* **353**, 470-474 (2016).
22. J. Ahn, E. J. Brook, Siple Dome ice reveals two modes of millennial CO_2 change during the last ice age. *Nat. Commun*. **5**, 3723 (2014).
23. T. K. Bauska, S. A. Marcott, E. J. Brook, Abrupt changes in the global carbon cycle during the last glacial period. *Nat. Geosci*. **14**, 91-96 (2021).
24. B. Riddell-Young, J. E. Lee, E. J. Brook, J. Schmitt, H. Fischer, T. K. Bauska, J. A. Menking, R. Iseli, J. R. Clark, Abrupt changes in biomass burning during the last glacial period. *Nature* **637**, 91-96 (2025).
25. K. A. Wendt, E. J. Brook, J. A. Higgins, J. E. Lee, J. A. Menking, T. S. Bauska, V. Gkinis, J. P. Severinghaus, Southern Ocean drives multidecadal atmospheric CO_2 rise during Heinrich Stadials. *Proc. Natl. Acad. Sci. U.S.A*. **121**, e2319652121 (2024).
26. V. Mariotti, L. Bopp, A. Tagliabue, M. Kageyama, D. Swingedouw, Marine productivity response to Heinrich events: a model-data comparison. *Clim. Past* **8**, 1581-1598 (2012).
27. L. Menviel, A. Timmermann, A. Mouchet, O. Timm, Meridional reorganizations of marine and terrestrial productivity during Heinrich events. *Paleoceanography* **23**, PA1203 (2008).
28. C. Reutenauer, A. Landais, T. Blunier, C. Breant, M. Kageyama, M.-N. Woillez, C. Risi, V. Mariotti, P. Braconnot, Quantifying molecular oxygen isotope variations during a Heinrich stadial. *Clim. Past* **11**, 1527-1551 (2015).
29. B. Luz, E. Barkan, M. L. Bender, M. H. Thiemens, K. A. Boering, Triple-isotope composition of atmospheric oxygen as a tracer of biosphere productivity. *Nature* **400**, 547-550 (1999).
30. T. Blunier, B. Barnett, M. L. Bender, M. B. Hendricks, Biological oxygen productivity during the last 60,000 years from triple oxygen isotope measurements. *Global Biogeochem. Cycles* **16**, 1029 (2002).
31. M. F. Miller, Isotopic fractionation and the quantification of ^{17}O anomalies in the oxygen three-isotope system: an appraisal and geochemical significance. *Geochim. Cosmochim. Acta* **66**, 1881-1889 (2002).
32. B. Luz, E. Barkan, The isotopic ratios $^{17}O/^{16}O$ and $^{18}O/^{16}O$ in molecular oxygen and their significance in biogeochemistry. *Geochim. Cosmochim. Acta* **69**, 1099-1110 (2005).
33. T. Blunier, M. L. Bender, B. Barnett, J. C. von Fischer, Planetary fertility during the past 400 ka based on the triple isotope composition of O_2 in trapped gases from the Vostok ice core. *Clim. Past* **8**, 1509-1526 (2012).
34. A. Landais, J. Lathiere, E. Barkan, B. Luz, Reconsidering the change in global biosphere productivity between the Last Glacial Maximum and present day from the triple oxygen

isotopic composition of air trapped in ice cores. *Global Biogeochem. Cycles* **21**, GB1025 (2007).
35. M. Brandon, A. Landais, S. Duchamp-Alphonse, V. Favre, L. Schmitz, H. Abrial, F. Prié, T. Extier, T. Blunier, Exceptionally high biosphere productivity at the beginning of Marine Isotopic Stage 11. *Nat. Commun*. **11**, 2112 (2020).
36. J.-W. Yang, M. Brandon, A. Landais, S. Duchamp-Alphonse, T. Blunier, F. Prié, T. Extier, Global biosphere primary productivity changes during the past eight glacial cycles. *Science* **375**, 1145-1151 (2022).
37. P. Sepulchre, A. Caubel, J.-B. Ladant, L. Bopp, O. Boucher, P. Braconnot, P. Brockmann, A. Cozic, Y. Donnadieu, J.-L. Dufresne, V. Estella-Pèrez, C. Ethé, F. Fluteau, M.-A. Foujols, G. Gastineau, J. Ghattas, D. Hauglustaine, F. Hourdin, M. Kageyama, M. Khodri, O. Marti, Y. Meurdesoif, J. Mignot, A.-C. Sarr, J. Servonnat, D. Swingedouw, S. Szopa, D. Tardif, IPSL-CM5A2 – an Earth system model designed for multi-millennial climate simulations. *Geosci. Model Dev*. **13**, 3011-3053 (2020).
38. M. L. Bender, T. Sowers, L. Labeyrie, The Dole effect and its variations during the last 130,000 years as measured in the Vostok ice core. *Global Biogeochem. Cycles* **8**, 363-376 (1994).
39. S. O. Rasmussen, P. M. Abbott, T. Blunier, A. J. Bourne, E. J. Brook, S. L. Buchardt, C. Buizert, J. Chappellaz, H. B. Clausen, E. Cook, D. Dahl-Jensen, S. M. Davies, M. Guillevic, S. Kopfstuhl, T. Laepple, I. K. Seierstad, J. P. Severinghaus, J. P. Steffensen, C. Stowasser, A. Svensson, P. Vallelonga, B. M. Vinther, F. Wilhelms, M. Winstrup, A first chronology for the North Greenland Eemian Ice Drilling (NEEM) ice core. *Clim. Past* **9**, 2713-2730 (2013).
40. J. Chappellaz, C. Stowasser, T. Blunier, D. Baslev-Clausen, E. J. Brook, R. Dallmayr, X. Faïn, J. E. Lee, L. E. Mitchell, O. Pascual, D. Romanini, J. Rosen, S. Schüpbach, High-resolution glacial and deglacial record of atmospheric methane by continuous-flow and laser spectrometer analysis along the NEEM ice core. *Clim. Past* **9**, 2579-2593 (2013).
41. R. H. Rhodes, E. J. Brook, J. C. H. Chiang, T. Blunier, O. J. Maselli, J. R. McConnell, D. Romanini, J. P. Severinghaus, Enhanced tropical methane production in response to iceberg discharge in the North Atlantic. *Science* **348**, 1016-1019 (2015).
42. V. Gkinis, S. B. Simonsen, S. L. Buchardt, J. W. C. White, B. M. Vinther, Water isotope diffusion rates from the NorthGRIP ice core for the last 16,000 years—Glaciological and paleoclimatic implications. Earth Planet. Sci. Lett. 405, 132–141 (2014).
43. T. K. Bauska, E. J. Brook, S. A. Marcott, D. Baggenstos, S. Shackleton, J. P. Severinghaus, V. V. Petrenko, Controls on Millennial-Scale Atmospheric CO_2 Variability During the Last Glacial Period. *Geophys. Res. Lett*. **45**, 7731-7740 (2018).
44. M. Guillevic, L. Bazin, A. Landais, C. Stowasser, V. Masson-Delmotte, T. Blunier, F. Eynaud, S. Falourd, E. Michel, B. Minster, T. Popp, F. Prié, B. M. Binther, Evidence for a three-phase sequence during Heinrich Stadial 4 using a multiproxy approach based on Greenland ice core records. *Clim. Past* **10**, 2115-2133 (2014).
45. J. P. Severinghaus, R. Beaudette, M. A. Headly, K. Taylor, E. J. Brook, Oxygen-18 of O_2 records the impact of abrupt climate change on the terrestrial biosphere. *Science* **324**, 1431–1434 (2009).
46. A. Seltzer, C. Buizert, D. Baggenstos, E. J. Brook, J. Ahn, J.-W. Yang, J. P. Severinghaus, Does $\delta^{18}O$ of O_2 record meridional shifts in tropical rainfall?, *Clim. Past* **13**, 1323-1338 (2017).
47. Y. L. Yung, W. B. DeMore, J. P. Pinto, Isotopic exchange between carbon dioxide and ozone via $O(^1D)$ in the stratosphere. *Geophys. Res. Lett*. **18**, 13–16 (1991).
48. J. Wen, M. Thiemens, Multi-isotope study of the $O(^1D) + CO_2$ exchange and stratospheric consequences. *J. Geophys. Res*. **98**, 12753–12758 (1993).

49. E. D. Young, L. Y. Yeung, I. E. Kohl, On the $\Delta^{17}O$ budget of atmospheric O_2, *Geochim. Cosmochim. Acta* **135**, 102-125 (2014).
50. N. Butchart, The Brewer-Dobson circulation, *Rev. Geophys*. **52**, 157-184 (2014).
51. L. Geng, L. T. Murray, L. J. Mickley, P. Lin, Q. Fu, A. J. Schauer, B. Alexander, Isotopic evidence of multiple controls on atmospheric oxidants over climate transitions, *Nature* **546**, 133-136 (2017).
52. E. L. Fleming, C. H. Jackman, R. S. Stolarski, A. R. Douglass, A model study of the impact of source gas changes on the stratosphere for 1850-2100, *Atmos. Chem. Phys*. **11**, 8515-8541 (2011).
53. J. L. Broccoli, D. M. Peteet, M. M. Mix, The response of the ITCZ to Northern Hemisphere cooling. *Geophys. Res. Lett*. **33**, L24703 (2006).
54. W. Chen, D. Zhu, P. Ciais, C. Huang, N. Viovy, M. Kageyama, Response of vegetation cover to CO_2 and climate changes between the Last Glacial Maximum and pre-industrial period in a dynamic global vegetation model. *Quat. Sci. Rev*. **218**, 293–305 (2019).
55. A. Schmittner, Decline of the marine ecosystem caused by a reduction in the Atlantic overturning circulation. *Nature* **434**, 628–633 (2005).
56. S. Albani, N. M. Mahowald, L. N. Murphy, R. Raiswell, J. K. Moore, R. F. Anderson, D. McGee, L. I. Bradtmiller, B. Delmonte, P. P. Hesse, P. A. Mayewski, Paleodust variability since the Last Glacial Maximum and implications for iron inputs to the ocean. *Geophys. Res. Lett.* **43**, 3944-3954 (2016).
57. L. N. Murphy, A. C. Clement, S. Albani, N. M. Mahowald, P. Swart, M. M. Arienzo, Simulated changes in atmospheric dust in response to a Heinrich stadial. *Paleoceanography* **29**, 30-43 (2014).
58. O. Aumont, C. Ethé, A. Tagliabue, L. Bopp, M. Gehlen, PISCES-v2: an ocean biogeochemical model for carbon and ecosystem studies. *Geosci. Model Dev*. **8**, 2465-2513 (2015).
59. S. P. Harrison, M. F. Sanchez-Goñi, Global patterns of vegetation response to millennial-scale variability and rapid climate change during the last glacial period, *Quat. Sci. Rev*. **29**, 2957-2980 (2010).
60. F. Pöppelmeier, A. Jeltsch-Thömmes, J. Lippold, F. Joos, T. F. Stocker, Multi-proxy constraints on Atlantic circulation dynamics since the last ice age, *Nature Geosci*. **16**, 349-356 (2023).
61. D. S. Goll, M. Bauters, H. Zhang, P. Ciais, Y. Balkanski, R. Wang, H. Verbeeck, Atmospheric phosphorus deposition amplifies carbon sinks in simulations of a tropical forest in Central Africa, *New Phytologist* **237**, 2054-2068 (2022).
62. R. Wang, D. Goll, Y. Balkanski, D. Hauglustaine, O. Boucher, P. Ciais, I. Janssens, J. Penuelas, B. Guenet, J. Sardans, L. Bopp, N. Vuichard, F. Zhou, B. Li, S. Piao, S. Peng, Y. Huang, S. Tao, Global forest carbon update due to nitrogen and phosphorus deposition from 1850 to 2100, *Glob. Change Biol*. **23**, 4854-4872 (2017).
63. M. Hein, K. Sand-Jensen, CO_2 increases oceanic primary production, *Nature* **388**, 526-527 (1997).
64. P. Schippers, M. Lürling, M. Scheffer, Increase of atmospheric CO_2 promotes phytoplankton productivity, *Ecol. Lett.* **7**, 446-451 (2004).
65. A. Cooper, C. S. M. Turney, J. Palmer, A. Hogg, M. McGlone, J. Wilmshurst, A. M. Lorrey, T. J. Heaton, J. M. Russell, K. McCracken, J. G. Anet, E. Rozanov, M. Friedel, I. Suter, T. Peter, R. Muscheler, F. Adolphi, A. Dosseto, J. T. Faith, P. Fenwick, C. J. Fogwill, K. Hughen, M. Lipson, J. Liu, N. Nowaczyk, E. Rainsley, C. Bronk Ramsey, P. Sebastianelli, Y. Souilmi, J. Stevenson, Z. Thomas, R. Tobler, R. Zech, A global environmental crisis 42,000 years ago. *Science* **371**, 811-818 (2021).

66. K. A. Wendt, A. D. Häuselmann, D. Fleitmann, A. E. Berry, X. Wang, A. S. Auler, H. Cheng, R. Lawrence Edwards, Three-phased Heinrich Stadial 4 recorded in NE Brazil stalagmites. *Earth Planet. Sci. Lett*. **510**, 94-102 (2019).
67. E. Barkan, B. Luz, High precision measurements of $^{17}O/^{16}O$ and $^{18}O/^{16}O$ ratios in H_2O. *Rapid Commun. Mass Spectrom*. **19**, 3737-3742 (2005).
68. C. Buizert, K. M. Cuffey, J. P. Severinghaus, D. Baggenstos, T. J. Fudge, E. J. Steig, B. R. Markle, M. Winstrup, R. H. Rhodes, E. J. Brook, T. A. Sowers, G. D. Clow, H. Cheng, R. L. Edwards, M. Sigl, J. R. McConnell, K. C. Taylor, The WAIS Divide deep ice core WD2014 chronology – Part 1: Methane synchronization (68-31 ka BP) and the gas age-ice age difference, *Clim. Past* **11**, 153-173 (2015).
69. B. Luz, E. Barkan, Proper estimation of marine gross O_2 production with $^{17}O/^{16}O$ and $^{18}O/^{16}O$ ratios of dissolved O_2, Geophys. Res. Lett. 38, L19606 (2011).
70. H. Craig, L. I. Gordon, Deuterium and oxygen-18 variations in the ocean and the marine atmosphere. in Stable Isotopes in Oceanographic Studies and Paleotemperatures, E. Tongiorgi, Ed. (Laboratorio di Geologia Nucleare, Pisa, 1965), pp. 9–130.
71. F. Joos, S. Gerber, I. C. Prentice, B. L. Otto-Bliesner, P. J. Valdes, Transient simulations of Holocene atmospheric carbon dioxide and terrestrial carbon since the Last Glacial Maximum. *Global Biogeochem. Cycles* **18**, GB2002 (2004).
72. S. von Caemmerer, *Biochemical Models of Leaf Photosynthesis* (CSIRO Publishing, Collingwood, Australia, 2000).
73. K. M. Grant, E. J. Rohling, M. Bar-Matthews, A. Ayalon, M. Medina-Elizalde, C. Bronk Ramsey, C. Satow, A. P. Roberts, Rapid coupling between ice volume and polar temperature over the past 150,000 years. *Nature* **491**, 744-747 (2012).
74. F. Hourdin, M.-A. Foujols, F. Codron, V. Guemas, J.-L. Dufresne, S. Bony, S. Denvil, L. Guez, F. Lott, J. Ghattas, P. Braconnot, O. Marti, Y. Meurdesoif, L. Bopp, Impact of the LMDZ atmospheric grid configuration on the climate and sensitivity of the IPSL-CM5A coupled model, *Clim. Dyn.* **40**(9-10), 2167-2192 (2012).
75. G. Krinner, N. Viovy, N. de Noblet-Ducoudré, J. Ogée, J. Polcher, P. Friedlingstein, P. Ciais, S. Sitch, I. C. Prentice, A dynamic global vegetation model for studies of the coupled atmosphere-biosphere system, *Global Biogeochem. Cycles* **19**, GB1015 (2005).
76. G. Madec, R. Bourdallé-Badie, P.-A. Bouttier, C. Bricaud, D. Bruciaferri, D. Calvert, D., J. Chanut, E. Clementi, A. Coward, D. Delrosso, C. Ethé, S. Flavoni, T. Graham, J. Harle, D. Iovino, D. Lea, C. Lévy, T. Lovato, N. Martin, S. Masson, S. Mocavero, J. Paul, C. Rousset, D. Storkey, A. Storto, M. Vancoppenolle, NEMO ocean engine (Version v3.6), in Notes Du Pôle De Modélisation De L'institut Pierre-simon Laplace (IPSL), Zenodo, https://doi.org/10.5281/zenodo.3248739
77. T. Fichefet, M. A. Morales Maqueda, Sensitivity of a global sea ice model to the treatment of ice thermodynamics and dynamics, *J. Geophys. Res*. **102**, 12609-12646 (1997).
78. S. Valcke, The OASIS3 coupler: a European climate modelling community software, *Geosci. Model Dev*. **6**, 373-388 (2013).
79. Y. Meurdesoif, A. Caubel, R. Lacroix, J. Dérouillat, M. H. Nguyen, XIOS tutorial, Retrieved from http://forge.ipsl.jussieu.fr/ioserver/raw-attachment/wiki/WikiStart/XIOS-tutorial.pdf.
80. G. Madec, M. Imbard, A global ocean mesh to overcome the North Pole singularity, *Clim. Dyn*. **12**, 381-388 (1996).
81. J.-L. Dufresne, M.-A. Foujols, S. Denvil, A. Caubel, O. Marti, O. Aumont, Y. Balkanski, S. Bekki, H. Bellenger, R. Benshila, S. Bony, L. Bopp, P. Braconnot, P. Brockmann, P. Cadule, F. Cheruy, F. Codron, A. Cozic, D. Cugnet, N. de Noblet, J.-P. Duvel, C. Ethé, L. Fairhead, T. Fichefet, S. Flavoni, P. Friedlingstein, J.-Y. Grandpeix, L. Guez, E. Guilyardi, D. Hauglustaine, F. Hourdin, A. Idelkadi, J. Ghattas, S. Joussaume, M.

Kageyame, G. Krinner, S. Labetoulle, A. Lahellec, M.-P. Lefebre, F. Lefevre, C. Lévy, Z. X. Li, J. Lloyd, F. Lott, G. Madec, M. Mancip, M. Marchand, S. Masson, Y. Meurdsoif, J. Mignot, I. Musat, S. Parouty, J. Polcher, C. Rio, M. Schulz, D. Swingedouw, S. Szopa, C. Talandier, P. Terray, N. Viovy, N. Vuichard, Climate change projections using the IPSL-CM5 Earth System Model: from CMIP3 to CMIP5, *Clim. Dyn*, **40**, 2123-2165 (2013).

82. B. S. Ferster, A. Simon, A. Ferorov, J. Mignot, E. Guilyardi, Slowdown and recovery of the Atlantic Meridional Overturning Circulation and a persistent North Atlantic Warming Hole induced by Arctic sea ice decline, *Geophys. Res. Lett*. **49**, e2022GL097967 (2022).
83. A.-C. Sarr, Y. Donnadieu, C. T. Bolton, J.-B. Ladant, A. Licht, F. Fluteau, M. Laugié, D. Tardif, G. Dupont-Nivet, Neogene South Asian monsoon rainfall and wind histories diverged due to topographic effects, *Nature Geosci*. **15**, 314-319 (2022).
84. M. Kageyama, S. P. Harrison, M.-L. Kapsch, M. Lofverstrom, J. M. Lora, U. Mikolajewicz, S. Sherriff-Tadano, T. Vadsaria, A. Abe-Ouchi, N. Bouttes, D. Chandan, L. J. Gregoire, R. F. Ivanovic, K. Izumi, A. N. LeGrande, F. Lhardy, G. Lohmann, P. A. Morozova, R. Ohgaito, A. Paul, W. Richard Peltier, C. J. Poulsen, A. Quiquet, D. M. Roche, X. Shi, J. E. Tierney, P. J. Valdes, E. Volodin, J. Zhu, The PMIP4 Last Glacial Maximum experiments: preliminary results and comparison with the PMIP3 simulations, *Clim. Past*, **17**, 1065-1089 (2021).
85. E. J. Gowan, X. Zhang, S. Khosravi, A. Rovere, P. Stocchi, A. L. C. Hughes, R. Gyllencreutz, J. Mangerud, J.-I. Svendsen, G. Lohmann, A new global ice sheet reconstruction for the past 80000 years, *Nat. Commun*. **12**, 1199 (2021).
86. M.-N. Woillez, G. Levavasseur, A.-L. Daniau, M. Kageyama, D. H. Urrego, M.-F. Sánchez-Goñi, V. Hanquiez, Impact of precession on the climate, vegetation and fire activity in southern Africa during MIS4. *Clim. Past* **10**, 1165-1182 (2014).
87. P. Le Mézo, L. Beaufort, L. Bopp, P. Braconnot, M. Kageyama, From monsoon to marine productivity in the Arabian Sea: insights from glacial and interglacial climates. *Clim. Past*, **13**, 759-778 (2017).
88. L. Bopp, K. E. Kohfeld, C. Le Quéré, O. Aumont, Dust impact on marine biota and atmospheric CO_2 during glacial periods, *Paleoceanography* **18**, 1046 (2003).
89. G. D. Farquhar, J. Lloyd, J. A. Taylor, L. B. Flanagan, J. P. Syvertsen, K. T. Hubick, S. C. Wong, J. R. Ehleringer, Vegetation effects on the isotope composition of oxygen in atmospheric CO_2, *Nature* **363**, 439-442 (1993).
90. W. J. Li, H. A. J. Meijer, The use of electrolysis for accurate $\delta^{17}O$ and $\delta^{18}O$ isotope measurements in water, *Isot. Environ. Health S*. **34**, 349-369 (1998).
91. Q. Fu, R. H. White, M. Wang, B. Alexander, S. Solomon, A. Gettelman, D. S. Battisti, P. Lin, The Brewer-Dobson Circulation during the Last Glacial Maximum, *Geophys. Res. Lett*. **47**, e2019GL086271 (2020).
92. D. A. Stolper, W. W. Fischer, M. L. Bender, Effects of temperature and carbon source on the isotopic fractionations associated with O_2 respiration for $^{17}O/^{16}O$ and $^{18}O/^{16}O$ ratios in *E. coli*, *Geochim. Cosmochim. Acta* **240**, 152-172 (2018).
93. B. Luz, E. Barkan, Net and gross oxygen production from O_2/Ar, $^{17}O/^{16}O$ and $^{18}O/^{16}O$ ratios, *Aquat. Microb. Ecol*. **56**, 133-145 (2009).
94. D. P. Nicholson, R. H. R. Stanley, E. Barkan, D. M. Karl, B. Luz, P. D. Quay, S. C. Doney, Evaluation triple oxygen isotope estimates of gross primary production at the Hawaii Ocean Time-series and Bermuda Atlantic Time-series Study sites, *J. Geophys. Res*. **117**, C05012 (2012).

Acknowledgments

We thank L. Bopp, W. Gray, S. Albani, E. Michel, and S. Harrison for their constructive advice. We are grateful to O. Marti, N. Vuichard, V. van Aalderen, and P. Sepulchre for

their support with the IPSL-CM5A2-VLR simulations. We also thank M. Döring, M. Kirk, I. Koldtoft, and J. P. Steffensen for their curation of the NEEM ice-core samples and their assistance with sample preparation and logistical support. NEEM is directed and organized by the Center of Ice and Climate at the Niels Bohr Institute and US NSF, Office of Polar Programs. It is supported by funding agencies and institutions in Belgium (FNRS-CFB and FWO), Canada (NRCan/GSC), China (CAS), Denmark (FIST), France (IPEV, CNRS/INSU, CEA and ANR), Germany (AWI), Iceland (RannIs), Japan (NIPR), Korea (KOPRI), The Netherlands (NWO/ALW), Sweden (VR), Switzerland (SNF), United Kingdom (NERC) and the USA (US NSF, Office of Polar Programs).

Funding:
European Union's Horizon 2020 research and innovation programme under the Marie Skłodowska-Curie grant agreement No 893105 (JWY, TB)
European Research Council under the European Union Horizon 2020 Programme grant agreement No 817493 (AL)
French National Research Agency grant ANR-22-CPJ1-0081-01 (JWY)
Grand équipement national de calcul intensif (GENCI) HPC computing hour allocations A0130102212, A0150102212 and A0170102212 (JBL, JWY)

Author contributions:

Conceptualization: JWY, TB, MK, AL, JBL
Methodology: AL, JBL, TB, MK, FP, SN, PB, JWY, NV, MFSG, LCM
Investigation: JWY, JBL, AL, TB, MK, DP, NV, PB, MFSG, LCM
Funding acquisition: JWY, TB, AL, JBL
Visualization: JWY, JBL, LCM, MK
Supervision: TB, AL, MK, DP, JWY
Writing—original draft: JWY, JBL, TB, AL, MK, DP
Writing—review & editing: JWY, TB, JBL, AL, MK, MFSG, DP, NV, PB, LCM

Competing interests: All other authors declare they have no competing interests.

Data and materials availability: All data are available in the main text or the supplementary materials. Data produced in the previous publications are publicly available in the following link: WAIS Divide CO_2 concentrations (https://www.pnas.org/doi/10.1073/pnas.2319652121), Taylor Glacier $\delta^{13}C\text{-}CO_2$ (https://www.ncei.noaa.gov/access/paleo-search/study/24170), NGRIP water stable isotope (https://doi.pangaea.de/10.1594/PANGAEA.886045), NEEM $^{17}O_{excess}$ and $\delta^{18}O_{atm}$ (http://dx.doi.org/10.5194/cp-10-2115-2014-supplement), and Siple Dome $\delta^{18}O_{atm}$ (https://www.usap-dc.org/view/dataset/609407).

Science Advances
AAAS

Supplementary Materials for

Global Biosphere Productivity Response to Atlantic Meridional overturning Circulation Collapse During Heinrich Stadial 4

Ji-Woong Yang *et al.*

*Corresponding author. Email: ji-woong.yang@lsce.ipsl.fr

This PDF file includes:

Supplementary Text
Figs. S1 to S12
Tables S1 to S2
Data S1
References (89 to 94)

Other Supplementary Materials for this manuscript include the following:

Data S1

Supplementary Text

Isotopic composition of source water in the box model

Modern values fractionation factors for precipitation water (equal to that of stem) and water vapor ${}^{18}\alpha_s$ and ${}^{18}\alpha_v$ are 0.9921 and 0.9818, respectively (*89*, *90*). To account for the past variability of the isotopic composition of the source water, we introduce a scaling factor (γ), which is expressed as a form of fractionation factor. In our box model, the isotopic composition of source water (R_s) and water vapor (R_v) are calculated as follows where x stands for s or v and $\theta = 0.528$ (*90*):

$${}^{18}R_x = {}^{18}\alpha_x \cdot \gamma(t) \cdot {}^{18}R_{sw}(t)$$

$${}^{17}R_x = \left({}^{18}\alpha_x \cdot \gamma(t)\right)^{\theta} \cdot {}^{17}R_{sw}(t) = {}^{17}\alpha_x \cdot \gamma(t)^{\theta} \cdot {}^{17}R_{sw}(t)$$

As consequence, the isotopic composition of the leaf water R_{lp} (*89*) is expressed as a function of time (t) and γ:

$$\begin{aligned}{}^{18}R_{lp}(t) &= \left[{}^{18}\alpha_s \cdot \gamma(t) \cdot {}^{18}\alpha_k \cdot (1-h) + {}^{18}\alpha_v \cdot \gamma(t) \cdot h\right] \cdot {}^{18}\alpha_{eq} \cdot {}^{18}R_{sw}(t) \\ &= {}^{18}\alpha_{lp}\gamma(t) \cdot {}^{18}R_{sw}(t)\end{aligned}$$

$$\begin{aligned}{}^{17}R_{lp}(t) &= \left[{}^{17}\alpha_s \cdot \gamma(t)^{0.528} \cdot {}^{17}\alpha_k \cdot (1-h) + {}^{17}\alpha_v \cdot \gamma(t)^{0.528} \cdot h\right] \cdot {}^{17}\alpha_{eq} \cdot {}^{17}R_{sw}(t) \\ &= {}^{17}\alpha_{lp}\gamma(t)^{\theta} \cdot {}^{17}R_{sw}(t)\end{aligned}$$

A box model can be formulated (*33*) for the isotopic composition of the troposphere which in steady state, $\frac{\mathrm{d}}{\mathrm{dt}}(M\ {}^{x}R_{atm}) = 0$, and modified for the time dependence of R_s and R_v writes as:

$${}^{17}R_{atm}(t) = \frac{F_{lp}(t) \cdot {}^{17}\alpha_{lp}\left(\gamma(t)^{\theta}\right) \cdot {}^{17}R_{sw}(t) + F_{op}(t) \cdot {}^{17}\alpha_{op} \cdot {}^{17}R_{sw}(t)}{F_{lp}(t) \cdot {}^{17}\alpha_{lr}(t) + F_{op}(t) \cdot {}^{17}\alpha_{or} \cdot {}^{17}\alpha_{ge} + F_{str}(t) \cdot \left(1 - {}^{17}\alpha_{str}\right)}$$

$${}^{18}R_{atm}(t) = \frac{F_{lp}(t) \cdot {}^{18}\alpha_{lp}(\gamma(t)) \cdot {}^{18}R_{sw}(t) + F_{op}(t) \cdot {}^{18}\alpha_{op} \cdot {}^{18}R_{sw}(t)}{F_{lp}(t) \cdot {}^{18}\alpha_{lr}(t) + F_{op}(t) \cdot {}^{18}\alpha_{or} \cdot {}^{18}\alpha_{ge} + F_{str}(t) \cdot \left(1 - {}^{18}\alpha_{str}\right)}$$

where $F_{lp}(t)$ and $\alpha_{lr}(t)$ are function of CO_2 concentrations. The ocean productivity $F_{op}(t)$ is then derived from both ${}^{17}R_{atm}$ and ${}^{18}R_{atm}$:

$$\begin{aligned}F_{op}(t) &= \frac{\left[F_{lp}(t) \cdot {}^{17}\alpha_{lr}(t) + F_{str}(t) \cdot \left(1 - {}^{17}\alpha_{str}\right)\right] \cdot {}^{17}R_{atm}(t) - F_{lp}(t) \cdot {}^{17}\alpha_{lp}\left(\gamma(t)^{\theta}\right) \cdot {}^{17}R_{sw}(t)}{{}^{17}\alpha_{op} \cdot {}^{17}R_{sw}(t) - {}^{17}\alpha_{or} \cdot {}^{17}\alpha_{ge} \cdot {}^{17}R_{atm}(t)} \\ &= \frac{\left[F_{lp}(t) \cdot {}^{18}\alpha_{lr}(t) + F_{str}(t) \cdot \left(1 - {}^{18}\alpha_{str}\right)\right] \cdot {}^{18}R_{atm}(t) - F_{lp}(t) \cdot {}^{18}\alpha_{lp}(\gamma(t)) \cdot {}^{18}R_{sw}(t)}{{}^{18}\alpha_{op} \cdot {}^{18}R_{sw}(t) - {}^{18}\alpha_{or} \cdot {}^{18}\alpha_{ge} \cdot {}^{18}R_{atm}(t)}\end{aligned}$$

The F_{op} calculated from ${}^{17}R_{atm}$ and ${}^{18}R_{atm}$ are equal. At each time step t above equation can be solved in two ways either by keeping $\gamma = 1$ and solving for h equaling similar meteoric conditions as today or by keeping h constant and solving for γ. Those scenarios are not exclusive a solution where both h and γ vary is possible maybe even likely. To solve the equation, we prescribe F_{lp} and F_{str} both are linked to the CO_2 concentration as described in Blunier *et al.* (*33*) and Yang *et al.* (*36*), respectively. With the solution for h or γ the isotopic composition of leaf water and F_{op} is calculated.

In previous studies (*33*, *36*) GOP-weighted relative humidity was varied while keeping the isotopic composition of source water constant. Here we favor the variable $\gamma(t)$ case. While no observational evidence is available so far, freshwater hosing experiments under LGM boundary conditions using IPSL-CM4 AOGCM show almost constant relative humidity (*28*). Also, our new experiments under 40 ka boundary conditions with the fully-coupled IPSL-CM5A2-VLR GCM indicate no significant change in relative humidity. Given those results, we keep relative humidity constant and turn to a time dependent fractionation of precipitation water and of water vapor.

Figure S1 shows the resulting ${}^{18}\varepsilon_{stem}$, and $\delta^{18}O$ of photosynthetic water ($\delta^{18}O_p$). The ${}^{18}\varepsilon_{stem}$ represents the isotopic fractionation effect of the photosynthetic source water from the global seawater. What is relevant to our box model approach is the GOP-weighted average value (temporally and spatially). Our box model predicts a gradual enrichment of $\delta^{18}O_p$ through the Period II in parallel to the ice-core $\delta^{18}O_{atm}$ records. This is consistent with Reutenauer *et al.*'s study (*28*) showing that the $\delta^{18}O_{atm}$ enrichment during HS is almost entirely explained by changes in $\delta^{18}O$ of precipitation water.

Figure S2 compares the global GOPs calculated by the two approaches. Both approaches result in an elevated GOP in Period II compared to Period I. Varying relative humidity shows a slightly dryer Period II. Monte-Carlo simulations calculating GOP from the CO_2-effect-corrected ${}^{17}\Delta$ curve and its probability distribution (red line and shaded area) yield less than 2% and 9% of solutions showing equal or lower GOP in Period II compared to Period I when varying humidity or gamma, respectively. This consistency reinforces the robustness of our finding that global biosphere productivity increases in Period II relative to Period I.

Sensitivity to stratospheric processes

Our box model does not include photochemical reactions of oxygen species in the stratosphere. The isotope fractionation effect in the stratosphere ($\epsilon_{str} = \alpha_{str} - 1$) is parameterized, scaling linearly with the past atmospheric CO_2 concentration. However, the ε_{str} value in the past is unknown and may not strictly follow CO_2 scaling. A sensitivity test with constant ε_{str} over periods I and II results in no GOP change (Figure S3). This result is not surprising since no compensation for CO_2-effect is needed by global biosphere. However, given the critical role of CO_2 in the depletion of heavy oxygen isotopes in O_2 (*47*), we consider the constant ε_{str} scenario unlikely and therefore favor our default scaling approach.

Another unknown is the past changes in the influx of stratospheric O_2 into the troposphere (F_{str}). Previous modelling study shows that with rising atmospheric CO_2 concentrations over the historical period the age of air (at 25 km altitude) decreases, implying an acceleration of Brewer-

Dobson Circulation (BDC) (*52*). We therefore scale F_{str} to CO_2 changes between 84.7% (CO_2 = 190 ppm) and 100% (CO_2 = 280 ppm) based on a climate-chemistry model simulation under LGM boundary conditions (*91*). Doing so, the abrupt CO_2 jump during HS4 leads to an increased influx of stratospheric O_2 with depleted $^{17}\Delta$ to the troposphere, implying that GOP reconstruction could be altered if the sensitivity of F_{str} to CO_2 changes. A sensitivity test of a constant F_{str} (fixed to the average value over Period I) leads to a weaker GOP rise in Period II compared to the default scenario. On average the observed relative change in GOP is only 1.2% (Figure S3). However, the triple oxygen isotopic ratio measurement in ice-core NO_3 suggest that BDC is accelerated under cold climate due to enhanced latitudinal gradient of SST (*e.g., 51*). If this is the case, a stronger BDC is more likely during HS4 because weakening AMOC causes a severe cooling around North Atlantic and hence greater latitudinal SST gradient, and is qualitatively consistent with our initial assumption. We therefore consider our default scenario more likely.

Sensitivity to prescribed land productivity

In our default scenario, we prescribe the land productivity in the identical manner to Blunier *et al.* (*33*), where the authors use a polynomial regression of simulated GPPC (*71*) to CO_2 concentration. The regression curve yields an increase in land GOP by ~2% in response to a CO_2 increase from 200 to 210 ppm. Our simulations using IPSL-CM5A2-VLR show an even stronger increase in land GOP of ~5% for a CO_2 increase from 200 to 210 ppm (experiments Exp_DUST and Exp_CO2). In order to examine the sensitivity of our box model calculating ocean GOP to prescribed land GOP, we carried out experiments using three different scenarios of prescribed land GOP. The double-sensitivity curve is obtained by following equation:

$$\text{Land biosphere GPPC (mol C } yr^{-1}) = -2.34 \times 10^{11} \times [CO_2]^2 + 1.55 \times 10^{14} \times [CO_2] - 1.26 \times 10^{16}$$

where $[CO_2]$ represents the CO_2 concentration in ppm. The land GOP curves used for sensitivity tests are shown in Figure S4. Given $^{17}R_{atm}$ and $^{18}R_{atm}$ (from ice-core $^{17}\Delta$ and $\delta^{18}O_{atm}$), the box model solutions yield a reduction of marine GOP in response to an enhancement in prescribed land GOP (Figure S4).

An increase in prescribed land GOP and concomitant decrease in marine GOP reduces the ocean-to-land GOP ratio (GOP_{oce}/GOP_{land}) and hence the $^{17}\Delta$ signature of photosynthetic O_2 produced in the global biosphere (Figure S4). A lower global biosphere $^{17}\Delta$ is compensated by a stronger GOP. The double-sensitivity scenario yields a 2.4% increase in global GOP in Period II (relative to Period I) compared to 1.9% in the default scenario (Figure S4).

In steady state, the reduced GOP_{oce}/GOP_{land} also affects the respiratory fractionation of ^{18}O, because of weaker terrestrial respiratory fractionation effect (~18 per mil) than that of marine biosphere (~21.5 per mil) prescribed in the box model. Given ice-core $\delta^{18}O_{atm}$ record, this 'deficit' of ^{18}O enrichment is compensated by an enrichment of ^{18}O in the source water (Figure S4).

Sensitivity to ^{17}O-anomaly of precipitation water

Another factor affecting the calculation of GOP is the ^{17}O anomaly of precipitation water as it affects the ^{17}O anomaly of photosynthetic O_2. What is relevant here is the GOP-weighted

average value. Due to the lack of direct observations, the GOP-weighted ^{17}O anomaly of precipitation water is kept constant in the default scenario. However, the high-resolution measurements of ^{17}O-excess from NEEM ice core samples demonstrate an abrupt shift by ~15 ppm from ~39.3 to ~38.6ka BP, likely reflecting rapid changes in low latitude hydrology (*44*). A sensitivity test in which the ^{17}O anomaly of precipitation water is reduced by 15 ppm over this interval results in even stronger biosphere productivity compared to the default scenario (Figure S5).

Sensitivity to C4 photosynthesis fraction

The fraction of C4 photosynthesis also influences our GOP calculations by altering the fraction of photorespiration and, consequently, the terrestrial respiratory fractionation factor. In the default scenario, the C4 fraction is scaled to CO_2 concentrations between 0.39 (LGM) and 0.275 (preindustrial), following Blunier *et al.* (*33*). This assumption results in an abrupt decline in the C4 fraction following the CO_2 increase. Maintaining a constant C4 fraction leads to a slight reduction in GOP during Period II, with 17% of 3000 Monte Carlo simulations showing a GOP decline in this period (Figure S5). However, recent ice-core measurements of stable CH_4 isotopes suggest increased biomass burning associated with the Heinrich Event (*24*). Such a scenario could shift the balance between C3 and C4 photosynthesis, as C4 plants (mainly in tropics) are likely more susceptible to wildfire. This would further reduce C4 photosynthesis. Thus, we consider a constant C4 contribution unlikely and conclude that any variations in C4 fraction between Periods I and II have a minor effect on GOP reconstruction.

Sensitivity to surface temperature

Soil- and marine respiratory isotopic effects can be altered by temperature change in response to HS4. According to our GCM simulations, the weighted (both in spatial and temporal) average of land surface temperature (Temp_sol) for land GOP is less than 1 degree between the control and freshwater perturbation experiments (slight warming). Similarly, the weighted average of the mean ocean temperature over the surface 100 meters for marine primary productivity is less than 1 degree between two experiments (slight warming). Land- and ocean surface warming by 1 degree will result in decrease in respiratory $^{18}\alpha$ values to 0.98379 (dark soil) and 0.97789 (ocean), while increase in the lambda value of marine respiration to 0.51819 (*33*, *92*). These changes have little effect on GOP calculation. In addition, the air-ocean equilibrium fractionation factors ($^{17}\alpha_{eq}$ and $^{18}\alpha_{eq}$) are functions of water temperature. Following the relationship by Luz and Barkan (*93*) and Nicholson *et al.* (*94*), the ocean surface warming by 1 degree induces decreases in $^{17}\alpha_{eq}$ and $^{18}\alpha_{eq}$ by 2 and 5×10^{-6}, respectively, and has little effect on reconstructed GOP.

Validation of simulated vegetation

We conduct our GCM experiments using a dynamic global vegetation model (DGVM) and validate the simulated vegetation by comparing it with available palynological data (*e.g., 59*). To facilitate this comparison, we first converted 11 plant functional types (PFTs) into 9 mega-biomes. The classification criteria and corresponding mega-biomes are summarized in Table S1. We compare the simulated vegetation in our Ctrl_40ka experiment with the pollen assemblage at GI 8, as a comprehensive pollen data compilation for 40 ka BP is not available (*59*). Overall, the simulated vegetation cover in the Ctrl_40ka experiment aligns well with pollen data, except along the western coast of America and in central Europe.

In America, the simulated vegetation on the east coast agree well with pollen data. On the west coast, the pollen records indicate a dispersion of boreal- and temperate forests, while the model simulates primarily 'Open Sclerophyll Forest/Woodlands' and 'Herbaceous and Shrublands', which are assigned a lower tree fraction than forest-type biomes (Table S1). This suggests that discrepancies between our DGVM and pollen data in this region arise from an underestimation of tree species in the model.

In East Asia, simulated vegetation cover closely matches pollen assemblages, except for one site in Southeast Asia where the model simulates 'Temperate Forest' instead of 'Warm Temperate Forest,' likely due to an underestimation of tropical tree species.

In Australia and New Zealand, the model simulates 'Bare Soil' and 'Herbaceous and Shrublands' in the interior of Australia, 'Tropical Savannah' and 'Open Sclerophyll Forest/Woodlands' along the northern coast, and 'Herbaceous and Shrublands' with 'Open Sclerophyll Forest/Woodlands' along the southern coast. However, it fails to capture tropical forest along the northern coast and tropical savannah in the south. Additionally, the model simulates 'Warm Tropical Forest' on the southern coast of Australia and in northern New Zealand, which is not reflected in pollen data.

In southern Europe, the model and pollen data are in good agreement, both showing a dominance of 'Open Sclerophyll Forest/Woodlands' and 'Herbaceous and Shrublands.' However, in central and eastern Europe, the model simulates 'Temperate Conifer and Broadleaf Forest,' whereas pollen data indicate a dominance of 'Herbaceous and Shrublands.'

Overall, we conclude that the model represents vegetation cover reasonably well in the Ctrl_40ka experiment, albeit with some spatial discrepancies. However, the pollen records are highly localized, limiting their ability to validate the simulation across the entire land surface. Notably, in South America—particularly in Amazonia—available pollen data provide little insight into this region. Our Ctrl_40ka simulation does not show well-developed tropical forest in the Amazon, likely due to a known bias in the IPSL-CM5A2-VLR model, which underestimates precipitation and forest cover over South America (*37*).

A comparison of vegetation simulated in the Exp_CO2 experiment with pollen records from GS 8/9 reveals several discrepancies. In western North America, the model fails to reproduce boreal and temperate forests indicated by pollen data, whereas the simulated temperate forest in eastern North America aligns well with observations (Figure S4). Similarly, along the western coast of South America, the model does not develop tree species (temperate conifer and broadleaf forests), instead simulating a dominance of herbaceous species.

In Europe, all data indicate a prevalence of 'Herbaceous and Shrublands,' yet the model simulates a widespread distribution of 'Open Sclerophyll Forest/Woodlands.' In Africa, the model predicts a mixture of tropical and temperate forests, whereas pollen records suggest a dominance of 'Open Sclerophyll Forest/Woodlands' and 'Herbaceous and Shrublands.' This discrepancy is likely due to an overestimated tree fraction, possibly linked to excessive simulated precipitation, as noted in pre-industrial experiments (*37*).

In Australia, the model fails to simulate tropical and temperate forests in the northern and eastern coastal regions. In contrast, the simulated vegetation cover in East Asia closely matches pollen assemblages. Overall, the Exp_CO2 experiment produces less coherent vegetation patterns compared to the Ctrl_40ka experiment.

<insert page break then Fig. S1 here>

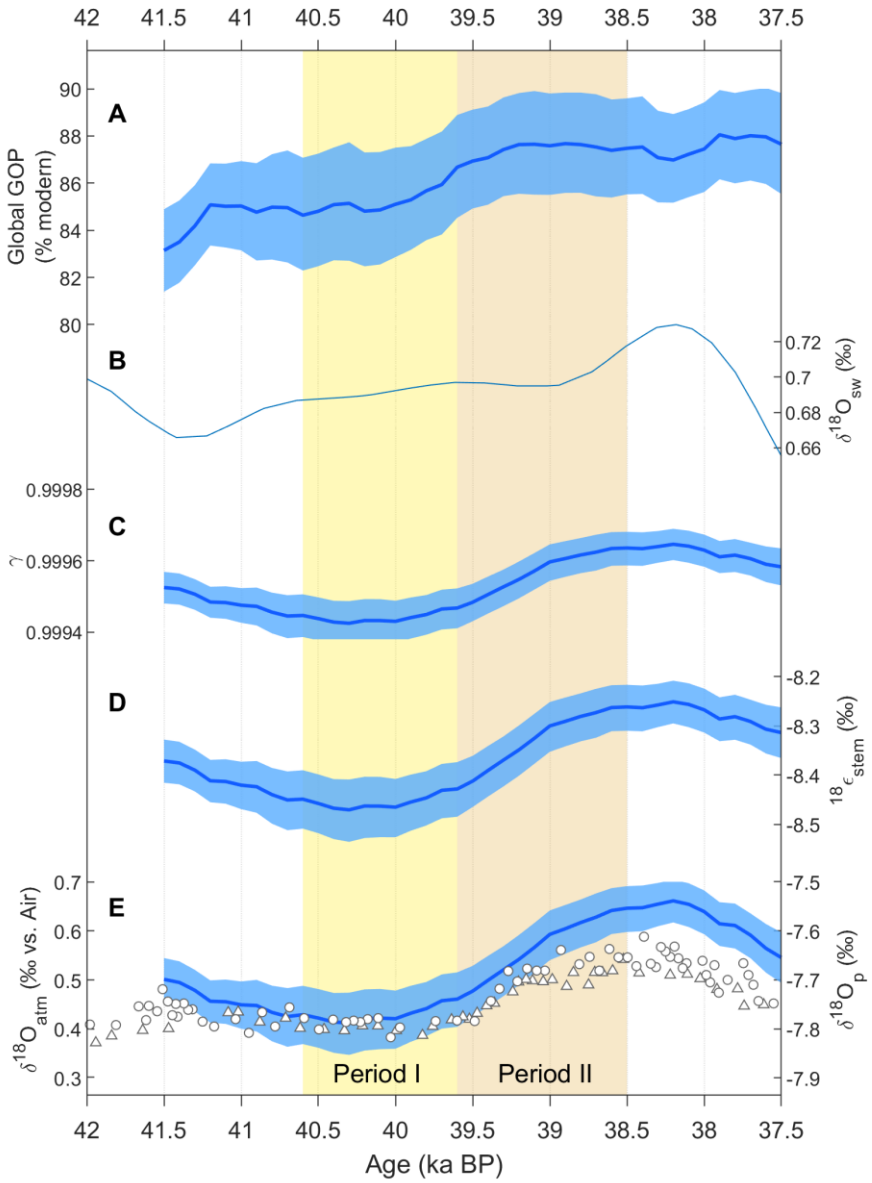

Fig. S1.
Results of "source-water approach" in our box model. (**A**) Reconstructed GOP in the default scenario. (**B**) The prescribed $\delta^{18}O_{sw}$ curve obtained by scaling the Red Sea relative sea-level record (*73*). (**C**) The gamma (γ) values calculated in the box model. (**D**) The GOP-weighted isotopic fractionation effect (expressed as $\varepsilon_{stem} = \alpha_{stem} - 1$) of precipitation water consumed by terrestrial plants versus global ocean water. (**E**) The isotopic ratio of precipitation water calculated in the box model and ice-core $\delta^{18}O_{atm}$ records (circles: NEEM; triangles: Siple Dome).

<insert page break then Fig. S2 here>

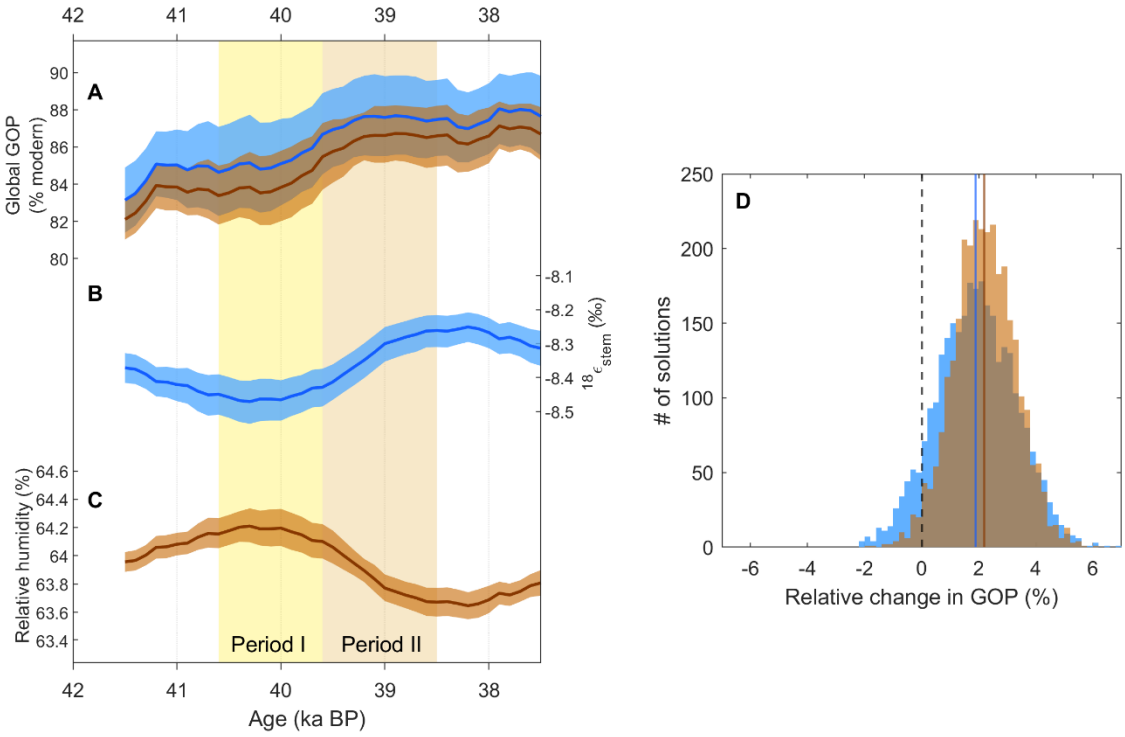

Fig. S2.

Comparison of the source-water approach (blue) and the relative-humidity approach (brown). (**A**) Reconstructed GOP records from both approaches. (**B**) The isotopic discrimination of GOP-weighted precipitation water. (**C**) The GOP-weighted relative humidity calculated in the box model. (**D**) The histogram of relative difference of GOP in Period II compared to that in Period I.

<insert page break then Fig. S3 here>

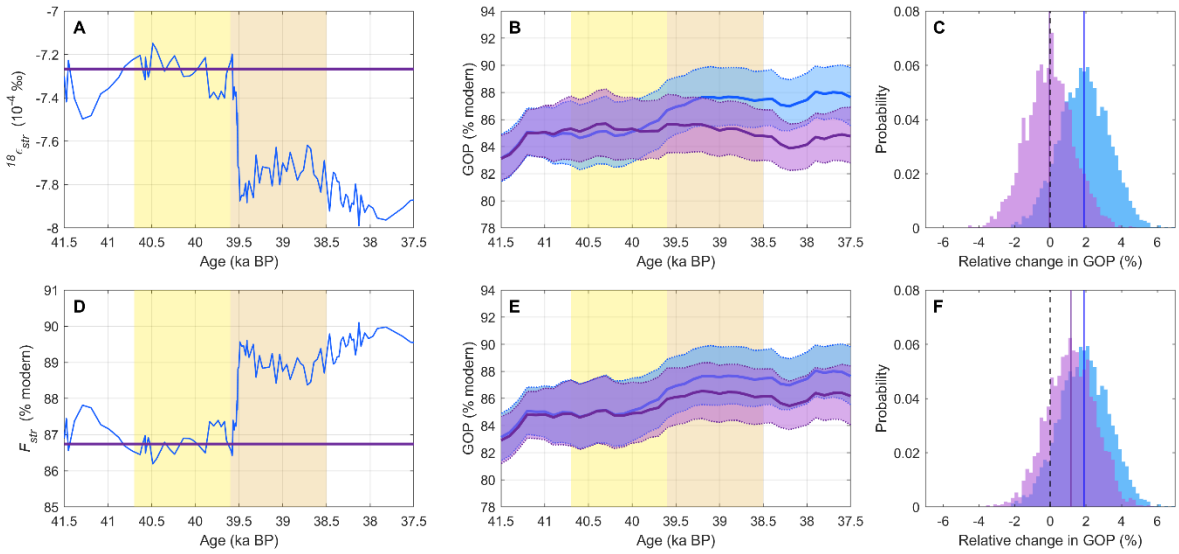

Fig. S3.

Sensitivity tests of GOP reconstruction for stratospheric processes. (**A** and **D**) The prescribed isotope fractionation effect in the stratosphere ($^{18}\varepsilon_{str}$) and the stratospheric influx to the troposphere (F_{str}). Blue curves indicate the default scenario and purple curves represent corresponding sensitivity experiment scenarios. (**B** and **E**) Comparison of resulting GOP. (**C** and **F**) Histogram of relative change of GOP between Period II and Period I. Yellow and orange shadings indicate Period I and Period II, respectively.

<insert page break then Fig. S4 here>

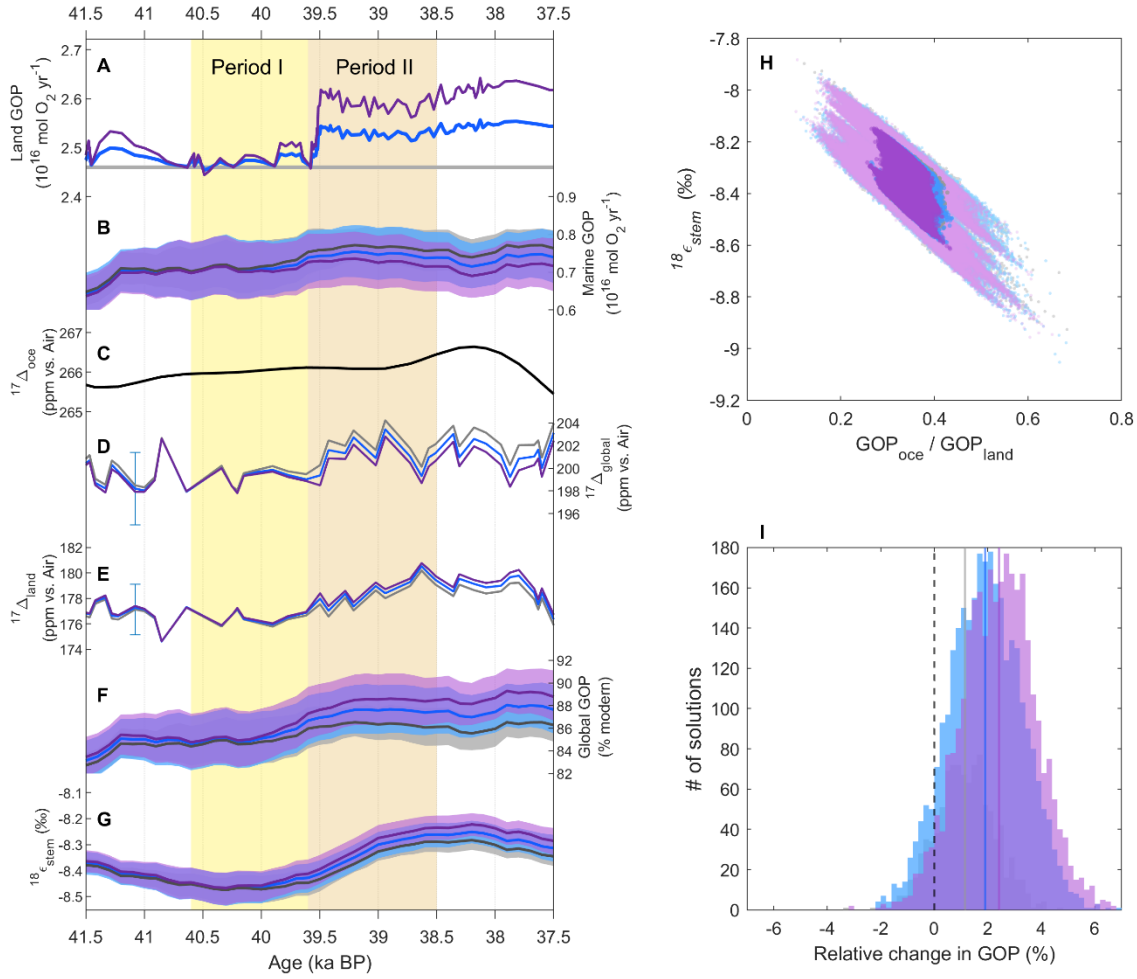

Fig. S4.

Sensitivity tests of GOP reconstruction for prescribed land productivity. (**A**) Different scenarios of prescribed land GOP. Blue curve is the default scenario, purple one represents the double-sensitivity case, and grey is constant land GOP scenario. (**B**) Calculated marine GOP in each scenario. (**C**) The $^{17}\Delta$ signature of marine photosynthetic O_2 ($^{17}\Delta_{oce}$). (**D**) The $^{17}\Delta$ signature of global photosynthetic O_2 ($^{17}\Delta_{global}$). (**E**) The $^{17}\Delta$ signature of terrestrial photosynthetic O_2 ($^{17}\Delta_{land}$). (**F**) Calculated global GOP and (**G**) isotopic composition of precipitation water. (**H**) The scatter plot of the ratio of oceanic- to terrestrial GOP to isotopic composition of precipitation water. (**I**) Comparison of relative change of GOP between Period II and Period I.

<insert page break then Fig. S5 here>

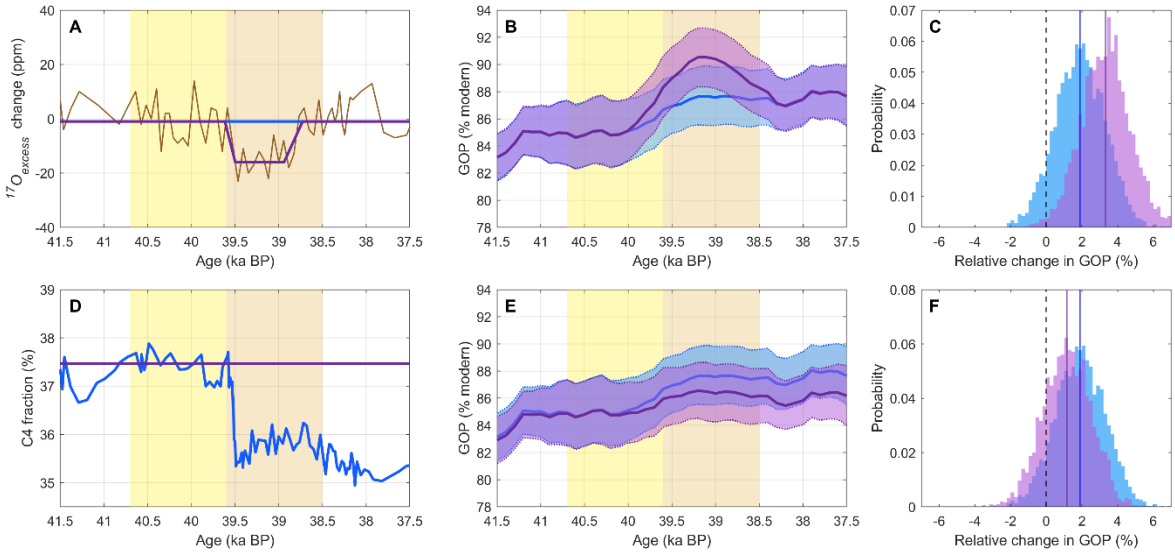

Fig. S5.

Sensitivity tests of GOP reconstruction for ^{17}O anomaly of precipitation water and fraction of C4 photosynthesis. (**A** and **D**) The prescribed ^{17}O anomaly ($^{17}O_{excess}$) and C4 photosynthesis fraction. Prescribed $^{17}O_{excess}$ are plotted as anomaly from the mean value over Period I. Blue curves indicate the default scenario and purple curves represent corresponding sensitivity experiment scenarios. Also plotted is the NEEM $^{17}O_{excess}$ record (*44*) expressed as anomaly from the mean value over the Period I. (**B** and **E**) Comparison of resulting GOP. (**C** and **F**) Histogram of relative change of GOP between Period II and Period I. Yellow and orange shadings indicate Period I and Period II, respectively.

<insert page break then Fig. S6 here>

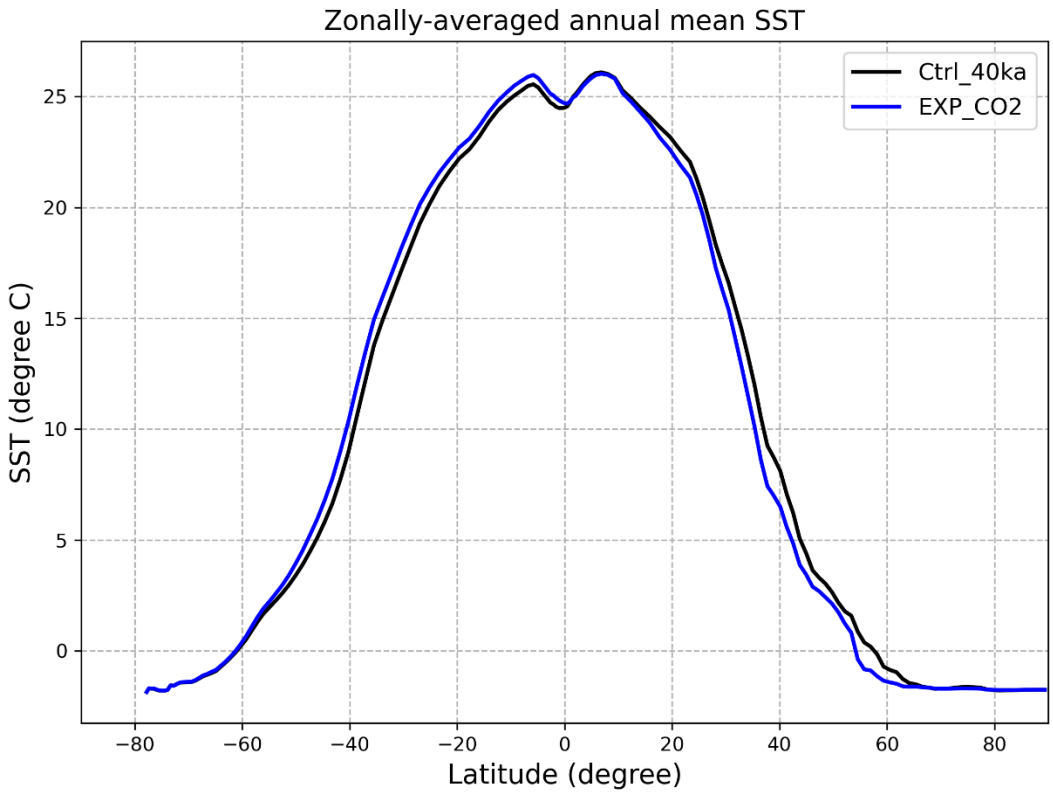

Fig. S6.
Latitudinal profiles of zonally-averaged annual mean SST obtained from Ctrl_40ka (black) and Exp_CO2 (blue) experiments using IPSL-CM5A2-VLR model.

<insert page break then Fig. S7 here>

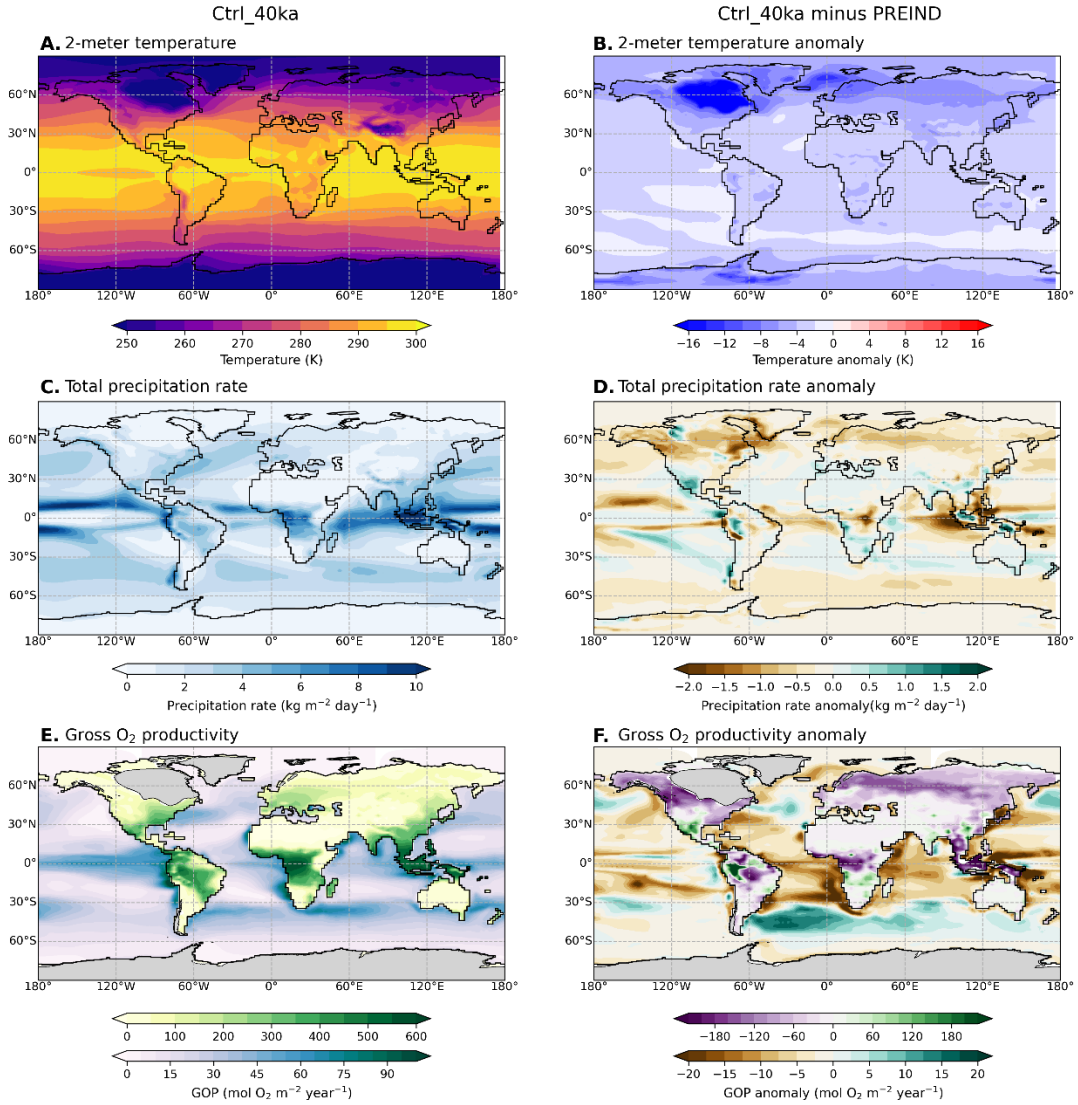

Fig. S7.

Simulated climate in our control experiment (Ctrl_40ka) and comparison with pre-industrial experiment (PREIND). (**A** and **B**) 2-meter temperature, (**C** and **D**) total precipitation rate, and (**E** and **F**) terrestrial- and oceanic gross O_2 productivity (GOP).

<insert page break then Fig. S8 here>

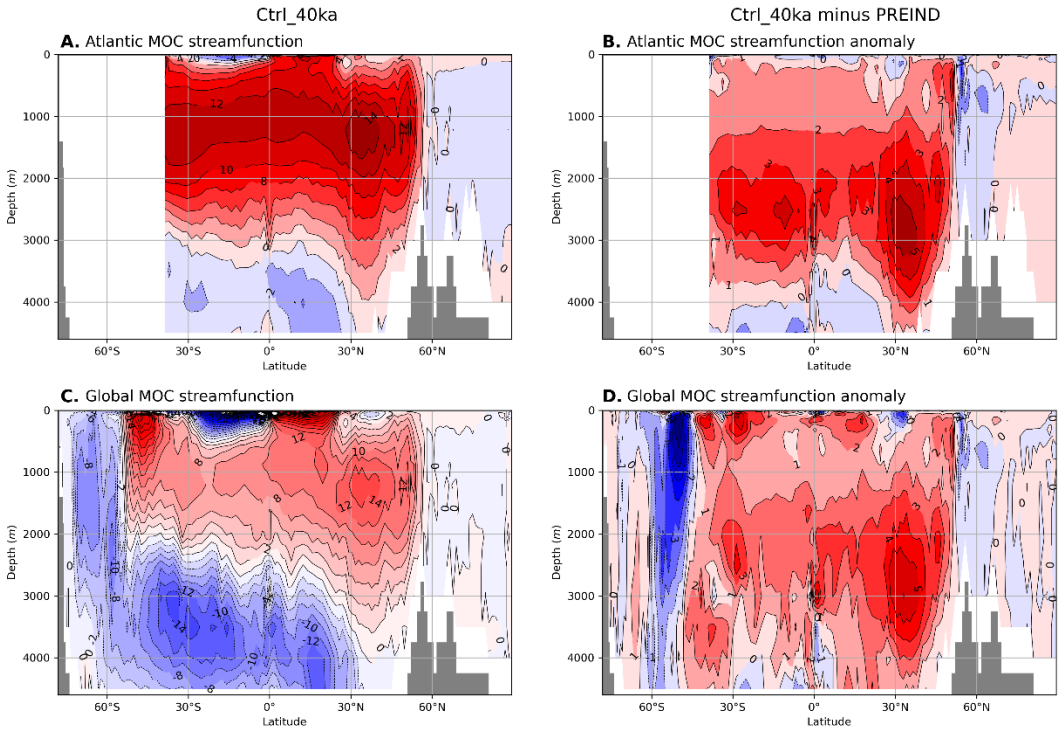

Fig. S8.

Simulated meridional overturning circulation in our control experiment (Ctrl_40ka) and comparison with pre-industrial experiment (PREIND). (**A** and **B**) stream function of Atlantic MOC, and (**C** and **D**) stream function of global MOC.

<insert page break then Fig. S9 here>

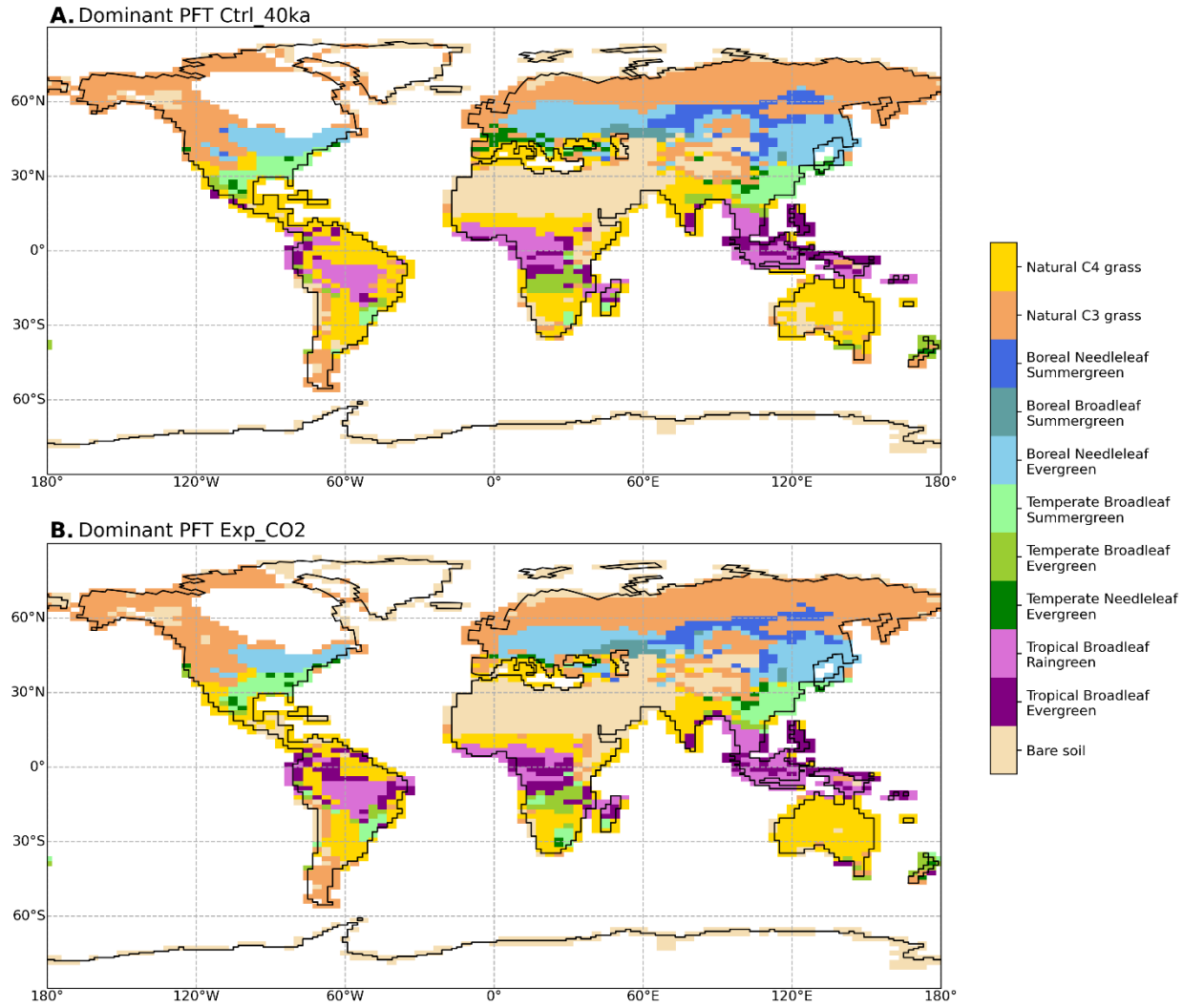

Fig. S9.

Comparison of dominant PFT simulated in Ctrl_40ka (upper) and Exp_CO2 experiments (lower).

<insert page break then Fig. S10 here>

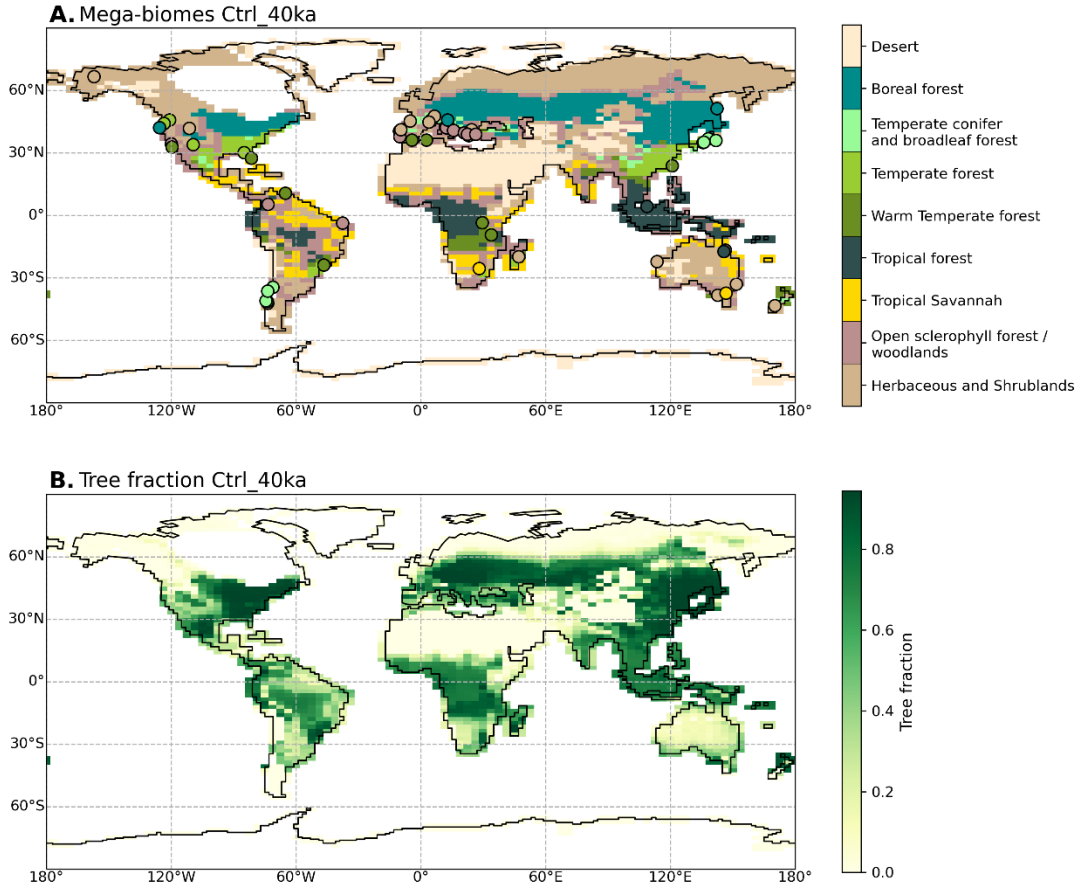

Fig. S10.

Simulated mega-biomes (upper) and tree fraction (lower) in Ctrl_40ka experiment. Mega-biome distribution is obtained by transforming simulated PFTs using criteria detailed in Table S1.

<insert page break then Fig. S11 here>

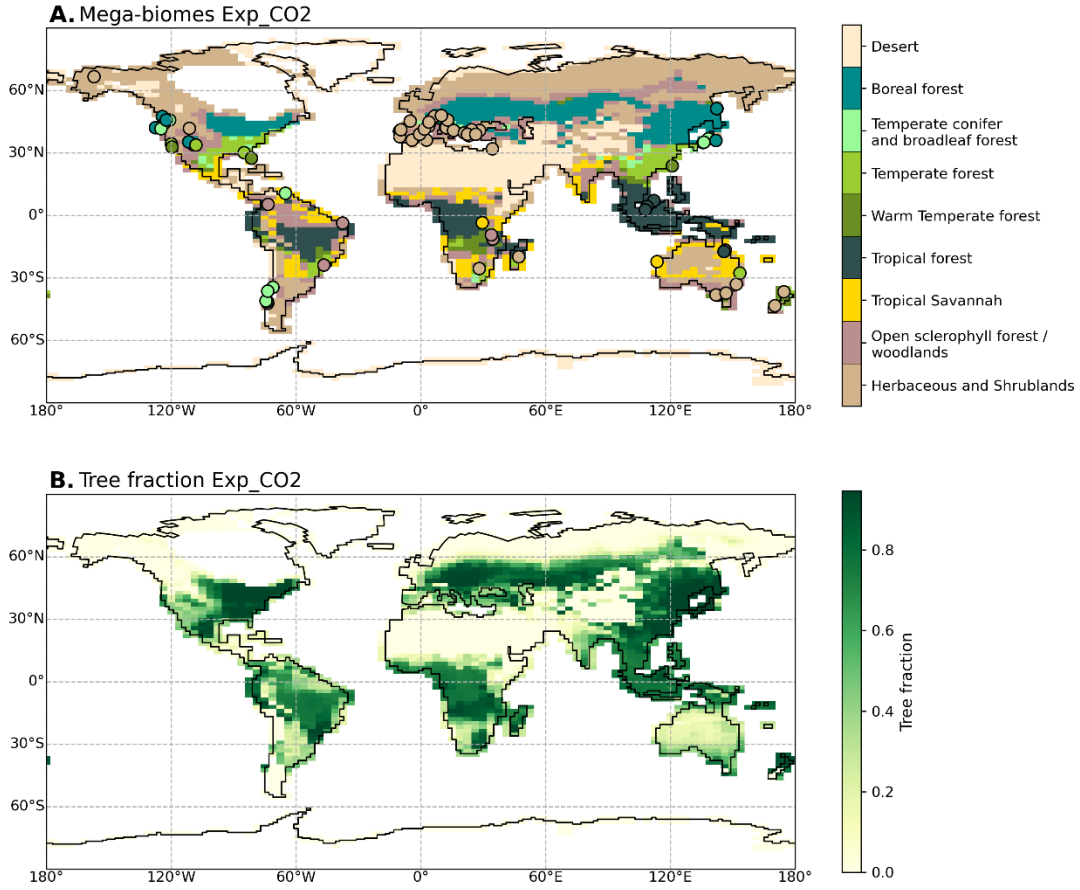

Fig. S11.

Simulated mega-biomes (upper) and tree fraction (lower) in Exp_CO2 experiment. Mega-biome distribution is obtained by transforming simulated PFTs using criteria detailed in Table S1.

<insert page break then Fig. S12 here>

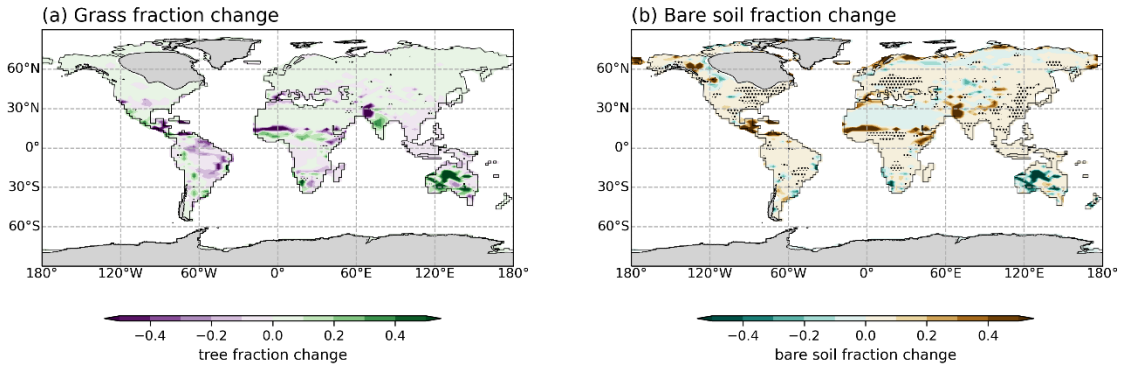

Fig. S12.

Changes in simulated (a) grass fraction and (b) bare soil fraction between Exp_CO2 and Ctrl_40ka experiments.

Table S1.

List of mega-biomes and criteria of conversion of PFT to mega-biomes.

Mega-biome	**Criteria**
Herbaceous and Shrublands	Tree fraction < 20% & Dominant PFT = Natural C3 grass or Natural C4 grass
	20% < Tree fraction < 40% & Dominant PFT = Natural C3 grass or Natural C4 grass or bare soil & Temperate or boreal region
Tropical savannah	20% < Tree fraction < 40% & Dominant PFT = Natural C3 grass or Natural C4 grass or bare soil & Tropical region
Open sclerophyll forest or woodlands	40% < Tree fraction < 70%
Tropical forest	Tree fraction > 70% & Dominant PFT = Tropical Broadleaf Evergreen Trees or Tropical Broadleaf Raingreen Trees or Natural C4 grass (for CTRL) or Natural C3 grass (for FWF) & Tropical region
Warm temperate forest	Tree fraction > 70% & Dominant PFT = Tropical Broadleaf Evergreen Trees or Tropical Broadleaf Raingreen Trees or Natural C3 grass or Natural C4 grass & Temperate region
	Tree fraction > 70% & Dominant PFT = Temperate Broadleaf Evergreen Trees
Temperate forest	Tree fraction > 70% & Temperate Broadleaf Summergreen Trees > 70%
Temperate conifer and Broadleaf forest	Tree fraction > 70% & Temperate Needleleaf Evergreen Trees > 20%
Boreal forest	Tree fraction > 70% & Dominant PFT = Boreal Needleleaf Evergreen Trees or Boreal Broadleaf Summergreen Trees or Boreal Needleleaf Summergreen Trees
Desert	Tree fraction < 20% & Dominant PFT = Bare soil

Table S2. Global biosphere productivity obtained in this study (in Pmol O_2 $year^{-1}$). The global productivity from ice-core data is calculated by multiplying the preindustrial GOP obtained from IPSL-CM5A2-VLR experiments. Relative changes in land, ocean, and global biosphere productivity with respect to Ctrl_40ka are given in parenthesis.

		Gross O_2 productivity (Pmol O_2 $year^{-1}$)				
		IPSL-CM5A2-VLR model			Ice-core data	
Experiment	Forcing	Land	Ocean	Global	Interval	Global
Ctrl_40ka	40ka	20.8 ± 0.4	8.8 ± 0.1	29.6 ± 0.6	Period I	29.7 ± 0.3
Exp_FWF	FWF	19.9 ± 0.3 (96 ± 2%)	8.5 ± 0.1 (96 ± 2%)	28.4 ± 0.6 (96 ± 3%)	-	-
Exp_DUST	FWF+dust	20.0 ± 0.3 (96 ± 2%)	8.6 ± 0.1 (97 ± 2%)	28.6 ± 0.6 (96 ± 3%)	-	-
Exp_CO2	FWF+dust+CO_2	21.0 ± 0.4 (102 ± 2%)	8.7 ± 0.1 (98 ± 2%)	29.7 ± 0.7 (100 ± 3%)	Period II	30.4 ± 0.2 (102 ± 1%)
Exp_VFIX	FWF+dust+CO_2 +fixed vegetation	21.3 ± 0.3 (103 ± 2%)	8.8 ± 0.1 (99 ± 2%)	30.1 ± 0.6 (102 ± 3%)	-	-

Data S1. (separate file)

The summary of $^{17}\Delta$ measurements of air O_2 trapped in the NEEM ice-core samples.

References

89. G. D. Farquhar, J. Lloyd, J. A. Taylor, L. B. Flanagan, J. P. Syvertsen, K. T. Hubick, S. C. Wong, J. R. Ehleringer, Vegetation effects on the isotope composition of oxygen in atmospheric CO_2, *Nature* **363**, 439-442 (1993).
90. W. J. Li, H. A. J. Meijer, The use of electrolysis for accurate $\delta^{17}O$ and $\delta^{18}O$ isotope measurements in water, *Isot. Environ. Health S.* **34**, 349-369 (1998).
91. Q. Fu, R. H. White, M. Wang, B. Alexander, S. Solomon, A. Gettelman, D. S. Battisti, P. Lin, The Brewer-Dobson Circulation during the Last Glacial Maximum, *Geophys. Res. Lett*. **47**, e2019GL086271 (2020).
92. D. A. Stolper, W. W. Fischer, M. L. Bender, Effects of temperature and carbon source on the isotopic fractionations associated with O_2 respiration for $^{17}O/^{16}O$ and $^{18}O/^{16}O$ ratios in *E. coli*, *Geochim. Cosmochim. Acta* **240**, 152-172 (2018).
93. B. Luz, E. Barkan, Net and gross oxygen production from O_2/Ar, $^{17}O/^{16}O$ and $^{18}O/^{16}O$ ratios, *Aquat. Microb. Ecol*. **56**, 133-145 (2009).
94. D. P. Nicholson, R. H. R. Stanley, E. Barkan, D. M. Karl, B. Luz, P. D. Quay, S. C. Doney, Evaluation triple oxygen isotope estimates of gross primary production at the Hawaii Ocean Time-series and Bermuda Atlantic Time-series Study sites, *J. Geophys. Res*. **117**, C05012 (2012).